We are IntechOpen,
the world's leading publisher of
Open Access books
Built by scientists, for scientists

6,100
Open access books available

167,000
International authors and editors

185M
Downloads

Our authors are among the

154
Countries delivered to

TOP 1%
most cited scientists

12.2%
Contributors from top 500 universities

CLARIVATE ANALYTICS
BOOK CITATION INDEX
INDEXED

WEB OF SCIENCE™

Selection of our books indexed in the Book Citation Index
in Web of Science™ Core Collection (BKCI)

Interested in publishing with us?
Contact book.department@intechopen.com

Chapter

The Influence of Geometry on Plasmonic Resonances in Surface- and Tip-Enhanced Raman Spectroscopy

Lu He, Dietrich R.T. Zahn and Teresa I. Madeira

Abstract

Plasmonic nanostructures have attracted growing interest over the last decades due to their efficiency in improving the performance in various application fields such as catalysis, photovoltaics, (opto-)electronic devices, and biomedicine. The behavior of a specific metal plasmonic system depends on many factors such as the material, the size, the shape, and the dielectric environment. The geometry, that is, size and shape of both single plasmonic elements and patterned arrays of plasmonic nanostructures, plays an essential role, and it provides considerable freedom to tune the plasmonic properties of a single plasmonic nanostructure or any combination of nanostructures. This freedom is mainly used in the application fields of surface-enhanced Raman spectroscopy (SERS) and tip-enhanced Raman spectroscopy (TERS). In this context, the chapter encompasses how the geometry of the SERS-active plasmonic nanostructures and tips with/without metal substrates used in TERS influences the localized surface plasmon resonances of the plasmonic systems.

1. Introduction

Almost 50 years ago, in 1974, Fleischmann et al. observed an enhanced Raman signal from a monolayer coverage of pyridine molecules adsorbed on a silver electrode [1]. Such unexpected behavior opened and initiated a new field of spectroscopic analysis including experimental and theoretical studies. Creighton's group [2] and Van Duyne's group [3] published similar results regarding pyridine molecules on silver anode surfaces using relatively low laser power and they brought forward different explanations for their results on the variation of Raman signal. Creighton explained that the enhanced signal is, on one hand, due to a surface effect increasing the molecular Raman scattering cross section and, on the other hand, due to the broadening of the electronic energy levels of molecules at rough metal surfaces, which may induce resonant Raman scattering from the adsorbed molecules *via* interaction with surface plasmons. Additionally, Van Duyne discovered that the enhancement of the

Raman signal is related to the roughness of the surface of the silver electrode and together they established the hypothesis that the phenomenon is due to electric field enhancement. Both explanations were accepted, but the electromagnetic enhancement was more prevailing [4] compared with the chemical or first-layer enhancement when molecules are in contact with metals.

In 1978, Moskovitz [5] put forward a possible explanation for the excitation-wavelength-dependent behavior observed by Creighton et al. [6] and Jeanmarie and Van Duyne [3]. He suggested that the observed behavior originates from the adsorbate-covered metal bumps on the metal surface, which could be considered as a two-dimensional colloid of metal spheres covered with the adsorbate and embedded in a dielectric medium on top of a smooth metal mirror. Additional absorption appears for those metal colloidal particles, for which interband electronic transitions exist [7].

Such resonance from the collective oscillation of conduction electrons on the metal surface and limited by the physical dimensions of the metal nanostructure is called localized surface plasmon resonance (LSPR). Typical metals used for plasmonic nanostructures are copper, silver, and gold [8, 9]. Due to the strong confinement of the electric field in the vicinity of such plasmonic metal nanostructures, they can be employed to break the optical diffraction limit and offer a vast range of applications in the fields of biology [10], chemistry [11–14], information [15], optical devices [16–19], and energy science [20, 21]. As a fast-developing field, researchers have studied plasmonic-related phenomena in all directions including the ultimate theoretical understanding from classical theory (e.g., Mie theory [22–26]) to quantum theory [27–29] aiming at providing a solid theoretical background to the main experimental and technological applications.

It is known that many factors, such as the material, size, shape, and dielectric environment, play important roles in determining the LSPR [30]. Among these factors, the geometry [31–37] of the plasmonic nanostructure provides the largest freedom and a straightforward way to tune the plasmonic resonance condition. Therefore, in this chapter, we focus on different geometries of plasmonic structures starting from introducing mathematical solutions for a single metal sphere representing a monomer system and two coupled metal spheres representing a dimer system. Then, we give a review on theoretical approaches that have been used in two powerful analytical techniques: SERS and TERS. Both experiment and simulation provide solid input to the understanding of the mechanisms and the principles of the techniques.

2. Theory on monomer and dimer systems

2.1 Single metal sphere: monomer systems

We refer to monomer systems when considering a single plasmonic nanostructure. Practically, for each system, in which metal nanoparticles are sparsely distributed in a dielectric environment, the interaction between the individual nanostructures can often be neglected so that each nanostructure can be considered as a monomer. Here, we address the equations for a single metal sphere regarding the light-matter interaction in detail [38–40], while the solution for further arbitrarily shaped single elements, which may appear more frequently in reality, is not derived, but related theoretical work can be found in refs. [41–46].

In the quasistatic approximation, light scattering by a spherical particle, the radius of which is a $(a \ll \lambda)$, in a uniformly distributed electric field of $E = E_0 r \cos \theta$
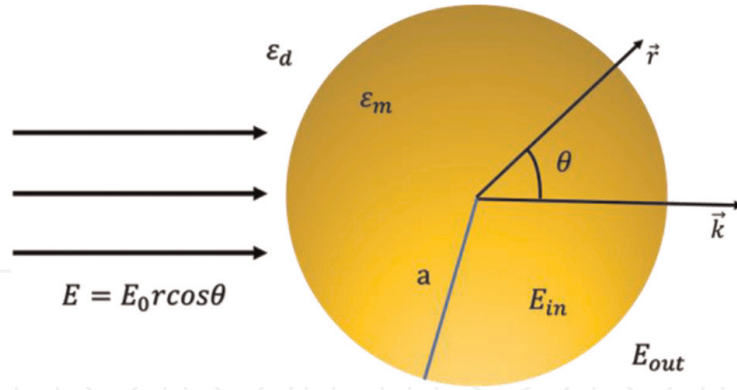
Figure 1.
Schematic sketch of a metal nanosphere in an electric field [38].

(as shown in **Figure 1** [40]) is described by the Laplace equations for the scalar electric potential [38].

$$E_{in} = -\nabla \Phi_{in} \tag{1}$$

$$E_{out} = -\nabla \Phi_{out} \tag{2}$$

$$\nabla^2 \phi_{in} = 0 \; (r < a) \tag{3}$$

$$\nabla^2 \phi_{out} = 0 \; (r > a) \tag{4}$$

with the continuous boundary conditions

$$\phi_{in} = \phi_{out}, \; \varepsilon_m \frac{\partial \phi_{in}}{\partial r} = \varepsilon_d \frac{\partial \phi_{out}}{\partial r} \; (r = a) \tag{5}$$

E_{in} and E_{out} indicate the electric fields inside and outside the metal particle with their electrical potential written as $\phi_{in}(r, \theta)$ and $\phi_{out}(r, \theta)$. ε_m and ε_d are the dielectric functions of the metal sphere and the dielectric environment, respectively. If we consider that the electric field at infinite distance is not disturbed by the metal sphere, the solution of Eqs. (1)–(4) can be written as [38].

$$\phi_{in} = \frac{-3\varepsilon_d}{\varepsilon_m + 2\varepsilon_d} E_0 r cos\theta \tag{6}$$

$$\phi_{out} = -E_0 r cos\theta + a^3 E_0 \frac{\varepsilon_m - \varepsilon_d}{\varepsilon_m + 2\varepsilon_d} \frac{cos\,\theta}{r^2} \tag{7}$$

Eq. (7) indicates that the potential outside the sphere can be considered as an addition of the incident field $-E_0 r cos\theta$ and a dipole with its dipole moment defined according to Eq. (8) [38],

$$p = 4\pi a^3 \varepsilon_0 \varepsilon_m \frac{\varepsilon_m - \varepsilon_d}{\varepsilon_m + 2\varepsilon_d} E_0 \tag{8}$$

with its polarizability α of [38]:

$$\alpha = 4\pi a^3 \frac{\varepsilon_m - \varepsilon_d}{\varepsilon_m + 2\varepsilon_d} \tag{9}$$

This is to say that we can consider a metal sphere, the dimension of which is much smaller than the wavelength of the incident light, as a simple dipole. Its polarizability is a function of the dielectric constant and size of the metal sphere.

Further derivation shows the cross sections for scattering and absorption are obtained from the scattered field radiated by this induced dipole interacting with the incident plane wave. They can be written as [38]:

$$C_{scattering} = \frac{k^4}{6\pi}|\alpha|^2 = \frac{8}{3}k^4\pi a^6 |\frac{\varepsilon_m - \varepsilon_d}{\varepsilon_m + 2\varepsilon_d}|^2 \tag{10}$$

$$C_{absorption} = kIm\{\alpha\} = 4k\pi a^3 Im\left\{\frac{\varepsilon_m - \varepsilon_d}{\varepsilon_m + 2\varepsilon_d}\right\} \tag{11}$$

where k is the wave vector of the incident light.

For a specific metal in a specific environment where ε_d and ε_m are defined and fixed, the absorption coefficient is proportional to the third power of the radius of the particle, while the scattering cross section is proportional to the sixth power of this radius. The efficiency of absorption dominates over the scattering efficiency when the particle size decreases.

Additionally, one can also notice a resonant enhancement for scattering and absorption when the condition $Re\,(\varepsilon_m + 2\varepsilon_d) = 0$ is satisfied, which is called Fröhlich condition [30]. This resonance is due to resonant excitation of the dipole surface plasmon. With the Drude model of the dielectric function, the frequency of the dipole surface plasmon can be written as $\omega_{sp} \approx \omega_p/\sqrt{3}$ with ω_p corresponding to the plasma frequency of the bulk metal.

The theory mentioned above can only be applied to particles that are much smaller than the excitation wavelength so that we can consider the electromagnetic field uniformly distributed across the entire metal particle. For particles with dimensions comparable to the excitation wavelength, in which the electrical field can no longer be considered uniform across the particle, a modified long wavelength approximation (MLWA) based on perturbative corrections has to be used [47–49].

The localized surface plasmon resonances (LSPRs) of noble metal particles with sizes of >10 nm were characterized well experimentally [50–53]. However, the characterization and understanding for sizes smaller than 10 nm is still poor and challenging from both experimental and theoretical points of view [54, 55]. This is mainly due to the fact that both quantum effects and surface interactions become important as the electrons interact more strongly with the surface including the spill-over of conduction electrons at the particle surface, which complicates geometrical analysis [56]; these effects cannot be described directly and solely by electrodynamics, and they require detailed calculations of the electronic structure for the actual atomic arrangements in the nanostructure of interest. In what concerns the experiments, the optical detection in the far field becomes difficult for small particles due to the size-dependent reduction in scattering intensity. In what concerns theory, time-dependent density functional theory-based methods are in general limited at present to particles with the sizes below 1–2 nm [57–59]. This mismatch between what can be achieved experimentally and what can be addressed theoretically make it difficult to benchmark both approaches.

2.2 Coupled elements: dimer systems

When we bring two or more single elements together, a new system is formed due to the interaction among those single elements and their light-matter interaction can

consequently be quite different. Here, we address a dimer system, which is composed of two metal spheres with a sufficiently small gap distance in the range of a few nanometers. These spheres are normally but not necessarily identical with respect to their size, geometry, and material.

A widely accepted and discussed theory stems from Nordlander [60], who gave an intuitive explanation to define the extinction cross section of dimer systems based on the gap distance between the nanoparticles. The dimer plasmons can be considered as a combination of bonding and antibonding states derived from the individual nanosphere plasmons. In this theory [61], the conduction electrons are considered as a charged and incompressible liquid sitting on top of rigid, positively charged ion cores. Ion cores are treated within the jellium approximation and the positive charge n_0 is uniformly distributed within the particle boundaries [62]. The plasmon modes are considered as self-sustained deformations of the electron liquid. Only the surface charges are responsible for such deformation since the liquid is incompressible. Therefore, the surface charge for a single solid metal sphere can be written as [61]:

$$\sigma(\Omega, t) = n_0 e \sum_{l,m} \sqrt{\frac{l}{R^3}} S_{lm}(t) Y_{lm}(\Omega) \tag{12}$$

where $Y_{lm}(\Omega)$ indicates the spherical harmonic of the solid angle Ω, R is the radius of sphere, S_{lm} represent the new degrees of freedom, and l is the angular momentum of a nanosphere. When the polar axis is chosen along the dimer axis, for a real representation that is adopted for the spherical harmonics, the interaction is diagonal in azimuthal quantum number m.

Therefore, the dynamics of the deformation is described by [61]:

$$L_s = \frac{n_0 m_e}{2} \sum \left[\dot{S}_{lm}^2 - \omega_{S,l}^2 S_{lm}^2 \right] \tag{13}$$

where $\omega_{S,l} = \omega_B \sqrt{\frac{l}{2l+1}}$ represents the solid sphere plasmon resonance and $\omega_B = \sqrt{\frac{e^2 n_0}{m_e \varepsilon_0}}$, represents the bulk plasmon frequency, $\dot{S}_{lm}$ represents the time derivative of the term S_{lm}. For the dimer system, when the distance between the centres of the two spheres is smaller than $\lambda_B/4$, retardation effects can be neglected and the dynamics of the plasmons is defined by the instantaneous Coulomb interaction between the surface charges as [61]:

$$V(D) = \int R_1^2 d\Omega_1 \int R_2^2 d\Omega_2 \frac{\sigma^1(\Omega_1)\sigma^2(\Omega_2)}{|\vec{r_1} - \vec{r_2}|} \tag{14}$$

where D is the separation between the centres of the two spheres in a dimer system.

The left panel in **Figure 2a** shows the dimer plasmon energies as a function of dimer separation for plasmon polarizations along the dimer axis ($m = 0$). At large separation, the interaction of plasmons on different nanoparticles is weak and the dimer plasmons are essentially bonding and antibonding combinations of plasmons of the same angular momentum l belonging to the nanoparticle.

When the separation is relatively large ($\sim$35 nm), the splitting of the bonding and antibonding dimer plasmons is symmetric. The splitting increases as their interaction increases. The bonding/antibonding configuration corresponds to the two dipole
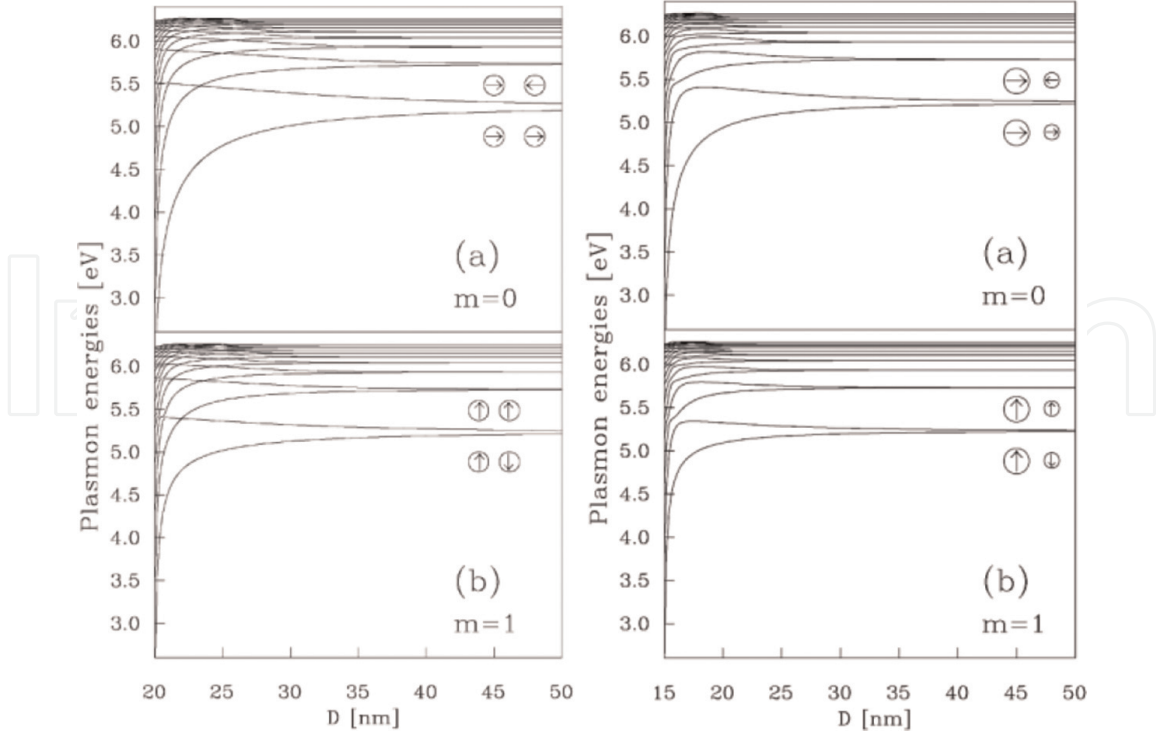
Figure 2.
Calculated plasmon energies of a nanosphere dimer with identical sphere radii of 10 nm as a function of interparticle separation (left); calculated plasmon energies of a heterodimer as a function of interparticle separation (right) with two spheres that have different radii of 10 nm and 5 nm. Panels (a) is for the azimuthal quantum number m = 0 and panels (b) for m = 1. The curves represent the bonding and antibonding dimer plasmons derived from the individual nanosphere plasmons with increasing angular momentum l. The arrows indicate the orientation of their dipole moments, see ref. [61].

moments moving in phase/out of phase (positive/negative parity of dipole moments or symmetric/asymmetric fields). For identical spheres, the net dipole moment of the negative parity plasmon (asymmetric field) is zero and they can hardly be excited by light, and they are therefore considered as dark plasmons, while the positive parity (symmetric field) plasmons are referred to as bright or luminous plasmons.

As the separation decreases, the splitting of $l = 1$ plasmon becomes asymmetric. Since the lower energy plasmon branch shifts faster than the higher energy plasmon branch, the overall non-dipole-like red shift effect is caused by the interaction of the $l = 1$ nanosphere plasmons with the higher l plasmons of the other nanosphere.

For the plasmons corresponding to $m = \pm 1$ (polarization-oriented perpendicular to the dimer axis shown in **Figure 2** left panel (b)), the overall phenomena are similar. Note that the assignment for the bright/dark plasmons is reversed in this case because the perpendicular polarization coupling has opposite signs.

The right panel of **Figure 2** depicts the dimer plasmon for a heterodimer as a function of dimer separation. The behavior with the separation is different compared with results shown in the left panel of **Figure 2**. As the parity of the dimer is broken, the lines representing the dimer plasmon energies exhibit avoided crossings in the figure. All dimer plasmons with $|m| \leq 1$ are bright.

As the separation decreases, the interactions get particularly strong when anti-bonding plasmons approach the bonding dimer plasmons of higher l manifolds, meaning that the higher l dimer plasmon also carries a finite dipole moment and becomes dipole active. Therefore, multiple peaks in the absorption spectra or a broad absorption region in the case of overlapping resonances are expected.

The result from the plasmon hybridization method is further compared with the finite difference time domain method (FDTD). And the results agree well with each other [63]. **Figure 3** from ref. [64] shows the scattering cross section of a nanosphere dimer system with radii of 40 nm and a separation distance varying from 0.5 to 200 nm compared with that of a monomer with a diameter of 80 nm. When the separation of the dimer is large, for example, 200 nm, the dimer system behaves the same as the monomer system, while decreasing the gap distance induces a shift toward higher energy and creating additional modes when the gap reaches 4 nm or even smaller distances.

Besides the above-mentioned hybridization method, another practical approach, which is used to describe coupled plasmon resonances in the so-called capacitive and conductive coupling regimes using an equivalent circuit model, was put forward by Benz et al. [65]. They claimed that such model can be used to calculate analytically the resonance wavelengths for different gap sizes, nanoparticle sizes, refractive indices, and linker conductivities.

To understand the dimer system further, different dimer systems are developed for fundamental studies. For example, Jeong et al. used an approach to fabricate plasmonic dimers in a very large scale with precise control of size, nanogap, material, and orientation [66]. They found that the optical response of each dimer is found to be identical with a highly uniform gap maintained across the array over centimeter distances. The existence of the transverse dipole mode and/or the longitudinal coupled resonance mode is highly dependent on the polarization of the incident light with respect to the dimer axis. A red shift can be observed with increasing gold nanoparticle size. Arbuz et al. recently studied the influence of the interparticle gap in dimers of gold nanoparticles on gold (Au), aluminum (Al), silver (Ag) films, and silicon (Si) wafers as substrates [67]. They claimed that the influence of the substrate vanishes when the dimer gap becomes larger than 2 nm. Nevertheless, the relation between the gap and the SERS intensity and enhancement factor is still under debate [68–71]. Also, Song et al. designed an experiment using an electromechanical method to tune the distance in the nm range between two Au nanoclusters as a strongly coupled plasmonic dimer, right before detrimental quantum effects set in. Different plasmon modes followed different trends as the bonding dipole (BDP) mode, a small blue shift
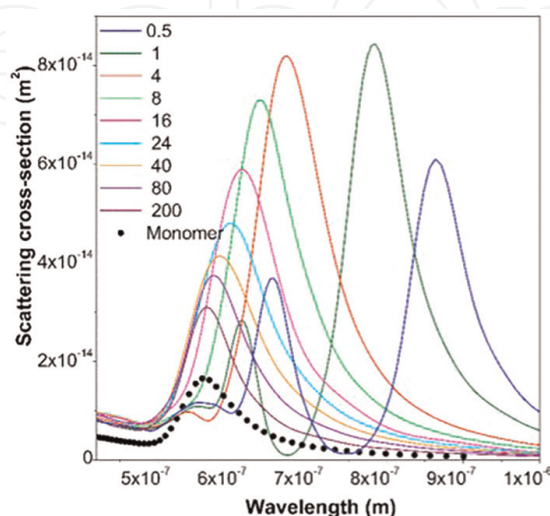

Figure 3.
FDTD simulation results for the scattering cross section of a nanosphere dimer system with radii of 40 nm and a separation distance varying from 0.5 to 200 nm compared with that of a monomer [64].

of the anti-bonding dipole (ADP) mode, and a negligible shift of anti-bonding vertical quadrupole (AVQP) mode with decreasing gap of the nanodisk dimer [72].

Dimer systems, as a basic metal nanostructure coupled system, provides a simple but very practical approximation for many application situations, especially in the two techniques, that is, SERS and TERS, that are discussed in the following sections.

2.3 Simulation on SERS and TERS

In the technical application of plasmonics, commonly used experimental configurations for SERS and TERS are shown in **Figure 4**. It is not only convenient but also reasonable to simplify the experimental configurations to simple spheres thus reducing a lot the computational cost in simulations. These schematic sketches of typical configurations include SERS in colloidal solution, SERS with a solid substrate, gap-mode SERS, TERS [73] and shell-isolated nanoparticle-enhanced Raman spectroscopy (SHINERS) [74–77].

To understand the impact of the geometry of plasmonic structures, simulations have an unbeatable advantage of freedom when designing the geometries. Besides straightforward experimental research, numerical simulations are gradually changing their role from a supporting approach to interpret the experimental results to a convenient and solid tool to investigate the mechanisms of plasmonic structures.

Various methods such as T-matrix [78–81], discrete dipole approximation (DDA) [82, 83], finite element method (FEM) [84, 85], and finite difference time domain (FDTD) [63, 64, 86] are used to address plasmonic systems. We can directly get the electric field distribution and use it for qualitative and even quantitative comparison with experiments. Classical theory based on solving Maxwell equations builds the backbone of many commonly used simulation tools while *ab initio* calculations may produce understanding beyond the knowledge obtained from classical theory. For a long time, we have tried to understand the mechanisms of light-matter interaction on metal nanoparticles. With the help of the fast development in the field of electronic and computer science, many computational methods were implemented to solve and
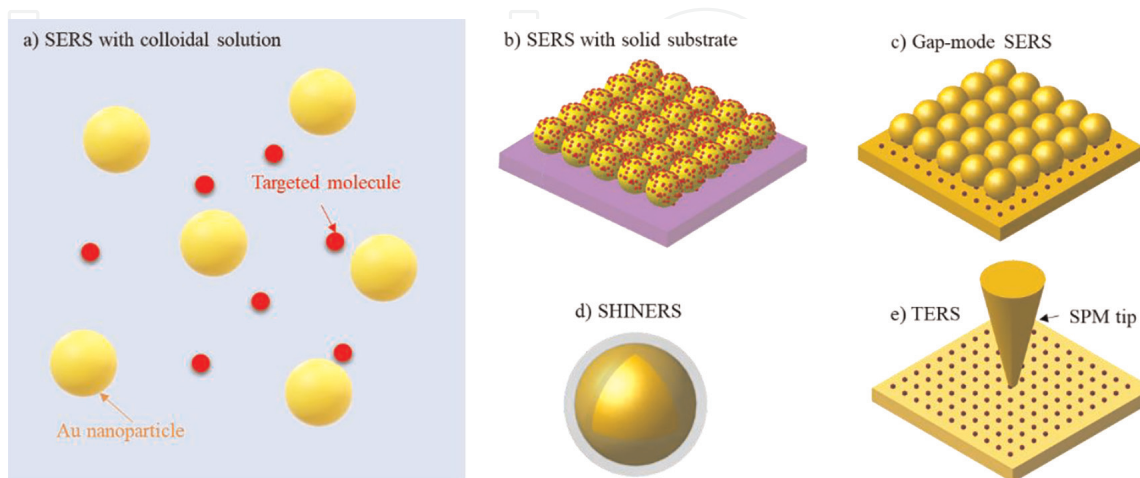

Figure 4.
Schematic presentations of different configurations of plasmon enhanced Raman spectroscopy. a) a plasmonic colloidal solution as a substrate for SERS. b) A plasmonic solid substrate for SERS, comprising a glass or silicon support and plasmonic metal nanoparticles. c) Gap-mode SERS. d) Shell-isolated nanoparticle-enhanced Raman spectroscopy (SHINERS) uses nanoparticles coated with a layer of a dielectric material. e) TERS, the nanoparticles are replaced by a single metallic scanning probe microscope (SPM) tip [73].

visualize this problem. As solving the Maxwell equations is the core mission in this field, solvers for a particular design have been developed in the form of either integral or differential equations [87, 88].

Table 1 [89] provides a comparison of the most used simulation tools for plasmonic structures.

Method	Computation Time for Au sphere with radius $<< \lambda$	Advantages	Disadvantages
Mie Theory	*Rapid*—a few milliseconds per individual frequency	• Rapid computation time.	• Applicable only to spherically symmetric particles.
		• Can also be used to compute the optical response of coated spheres.	• Not possible to include a substrate interaction, therefore difficult to replicate many experiments.
T-Matrix	*Rapid*—a few milliseconds—per individual frequency.	• Rapid computation time.	• Computations are numerically unstable for elongated or flattened objects (the matrices are truncated during computation—rounding errors become significant and accumulate rapidly)
		• Wide range of geometries supported.	
		• Also possible to include a substrate interaction	
DDA	*Moderate*—depends on number of dipoles, and separation. Typically 50s per individual frequency.	• Can be used to evaluate any arbitrary-shaped particle by specifying a tabulated list of dipole locations	• Convergence criterion: $\|n\|kd < 1$ n = complex refractive index k = wavevector d = inter-dipole separation (Not possible to solve for high aspect ratio / elongated particles, or those having a large refractive index)
FEM	*Lengthy*—typically 150 s per individual frequency when using an element length of 3 nm. A compromise is made between the computation time and element length.	• Can be used to evaluate the scattered field distribution of any arbitrary-shaped particle.	• Computation time is lengthy.
		• The use of a non-regular tetrahedral adaptive mesh for the FEM simulation allows for a more accurate approximation of curved surfaces.	
FDTD	*Lengthy*—a broadband response is computed across a wide frequency range, typically taking $\approx$ 3 hours to cover visible frequencies. A compromise made between the computation lime and element length.	• Can be used to evaluate scattering parameters from any arbitrary-shaped panicle.	• Computation time is lengthy.
			• Permittivity values have to be specified over much wider frequency range than just the range of interest. The Drude-Lorentz model may not be an accurate representation of experimental data.

Table 1.
Comparison on computation time, advantages, and disadvantages of different computational techniques [89].

Among above-mentioned simulation methods, the finite element method (FEM) and the finite difference time domain (FDTD) method are the most commonly and widely used methods commercially available nowadays. In brief, FEM reduces the complex partial differential equations to simple algebraic equations. This method gives the approximate results at each discrete number of points over the domain. To solve the problem, it divides the whole problem into various numbers of discrete units generally termed as mesh elements. FEM can be applied to various physical problems such as structural analysis, fluid flow, electromagnetic potential, and mass transport [90]. FDTD, on the other hand, is usually suitable to solve transient change processes of a field under external excitation. If a pulsed excitation source is used, a single solution can yield a response over a wide-frequency band. Time domain methods have reliable accuracy and faster computational speed, and can truly reflect the nature of electromagnetic phenomena, especially in research areas requiring time domain measurements [91]. FDTD is more useful for nonlinear materials with offering a large range of wavelength-dependent dielectric constants and broadband simulations especially for the transient studies, while FEM benefits from unstructured gridding and is therefore more promising for higher-order curved elements with the advanced FEM codes [89, 92].

One of the most used simulation tools based on the FEM method is COMSOL Multiphysics [93]. This software includes various working packages for a variety of applications, among which the Wave Optics module is the one specifically used for plasmonic studies, because it enables to handle objects, the dimensions of which are comparable or smaller than the probing wavelength [94]. All modeling formulations are based on Maxwell's equations together with material laws for propagation in various media. The modeling capabilities are accessed *via* predefined physics interfaces, which allow the user to set up and solve the electromagnetic models in two- and three-dimensional spaces. The modeling of electromagnetic fields and waves can be performed in the frequency domain, time domain, eigenfrequency, and mode analysis. The modeling typically follows the sequence: definition of the geometry, selection of materials, selection of a suitable Wave Optics interface, definition of boundaries and initial conditions, definition of the finite element mesh, selection of a solver, and visualization of the results [94]. Most of the simulations presented in both SERS and TERS sections were performed with this tool.

2.3.1 SERS

In the typical SERS configuration shown in **Figure 4a**, computer simulations showed that spherical Au and Ag NPs as monomers cannot generate a strong localized electric field on their surface [95], and nevertheless, they carry on being most widely used options in SERS and TERS experiments, where high-quality signals can be obtained from different analytes, due to their easy and fast synthesis. Since a main task in SERS and TERS research is to increase the sensitivity of the plasmonic systems, other alternative geometric structures have been investigated, in which the aspect ratio of the spheroid structures is investigated: particles with prolate or oblate spheroid geometries [96]. A practical approximation in ref. [97] shows the possibility to use a Taylor expansion to numerically predict the extinction spectra of metallic spheroidal particles for a wide range of the geometric aspect ratios.

For configurations as shown in **Figure 4b** and **c**, classical electrodynamics provides a good description down to gap distances of the order of >1 nm, after which quantum and non-local theory approaches have to be used [98–100]. The EM enhancement

continues until the distance between two metal surfaces becomes so small that electron spill-out and non-local effects become important, eventually leading to electronic tunneling and electrical shortcut [101]. Such phenomena are observed by simply bringing two or more spherical NPs close enough experimentally [102–104].

It is worth to mention that besides the spherical nanostructures in **Figure 4** other nanostructures, such as mesoporous gold particles [105], nanostars/flowers [106–113] or spiky structures/superstructures [114, 115], nanoshells [116], nanocubes [117–122], and hollow-structured particles [109, 112], have been considered. For those as SERS substrates, their edges work as hotspots concentrating the electromagnetic field of the probing light into small volumes. This enhances the local electromagnetic (EM) field near the edges of these metal nanostructures. The "hotspot" areas utilize the field enhancement properties of the metal nanostructures to amplify the usually weak Raman scattering signals.

Another way to boost the hotspots is to bring two or more particles in close vicinity. Therefore, many agglomerated structures are practically used to increase the SERS enhancement employing the interaction among the single monomers to fulfill the "dimer" condition, such as clusters [123], trimers [67, 124–128], tetramers [125, 129, 130], chains [131, 132], and arrays [133–137]. Detailed studies to understand such agglomerates were performed by several groups. Sergiienko et al. investigated the influence of NP agglomeration on the SERS signal [127]. The study was carried out on monomers, dimers, and trimers. In comparison with a single NP, the plasmonic absorption for dimers exhibits a new band at longer wavelength (red shift) due to the interparticle plasmonic coupling. Theoretically, the interparticle plasmonic coupling leads to more enhancement and red shifts the plasmonic absorption band with increasing degree of aggregation. When the nanoparticles in a chain are brought closer to each other (gaps decreasing from 2.5 to 0.5 nm), the maximum field enhancement at the gap becomes nearly 10 times larger and aggregation causes a large red shift of more than 200 nm. Overall, the SERS enhancement factor (EF) increases by 43% in average upon dimerization and 96% upon trimerization for both AuNPs and AgNPs. However, the maximum ratio of EFs for some dimers to the mean EF of monomers can be as high as 5.5 for AgNPs on gold substrates. For dimerization and trimerization of gold and silver NPs on silicon, the mean EF increases by 1–2 orders of magnitude relative to the mean EF of single NPs. Therefore, the hotspots in the interparticle gap between gold nanoparticles rather than hotspots between Au nanoparticles and substrate dominate the SERS enhancement for dimers and trimers on a silicon substrate. Raman-labeled noble metal nanoparticles on plasmonic metal films generate on average SERS enhancement of the same order of magnitude for both types of hotspot zones (i.e., NP/NP and NP/metal film). A summary of these results is presented in **Figure 5**. More details about this work can be found in ref. [124]

A SERS substrate can be composed of both monomer and dimer metal structures placed on metal/non-metal substrates. Arrays, as one of the important configurations, have been utilized in many fields [66, 138–140]. The fabrication of plasmonic arrays is also versatile including both top-down and bottom-up methods as described, for example, in ref. [138] and for instance, nanogap arrays using photolithography for nanogap arrays with swelling-induced nano-cracking [141], superimposition metal sputtering [135], and direct writing [142].

Among such methods, the so-called nanosphere lithography (NSL) using self-assembled nanospheres as a shadow mask for metal deposition is a typical cost-efficient and fast technique [143, 144]. NSL details are reviewed elsewhere [145]. Various metals can be used, such as silver, gold, copper, and aluminum. SEM images
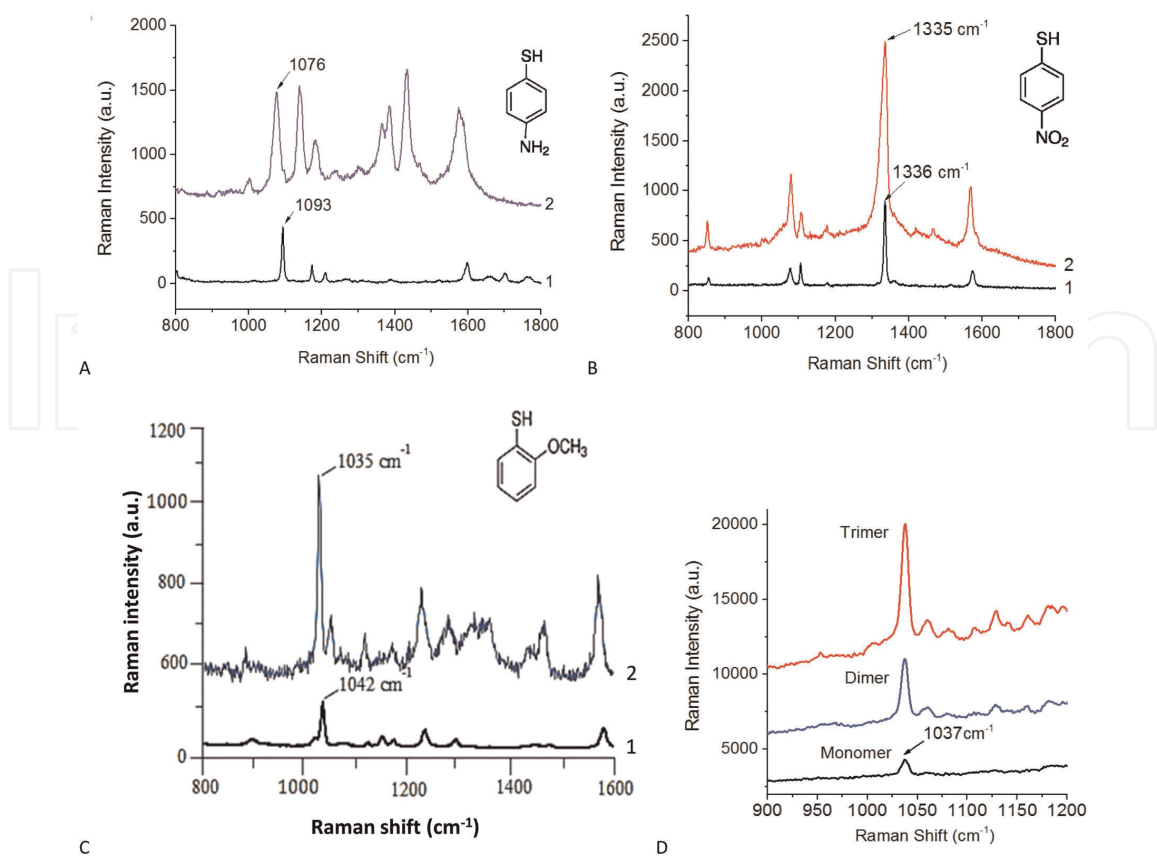
Figure 5.
Raman and SERS spectra of analytes adsorbed on 60 nm Au NPs on an Au film: (A) 4-aminothiophenol, 1—Raman, 2—SERS, (B) 4-nitrobenzenethiol, 1—Raman, 2—SERS, (C) 2-methoxythiophenol, 1—Raman, 2—SERS, (D) SERS spectra of 2-methoxythiophenol (monomer, dimer, and trimer) [127].

of such typical structures are shown in **Figure 6**. Tuning the plasmon resonance frequency of such structure can be performed in the range from the near infrared to the blue spectral using different metals and by annealing them at different temperatures [146]. This tuning is simply based on the change of the shape of each metal nanotriangle (NT) from triangular to roundish for the case of Au and Ag. For Cu and
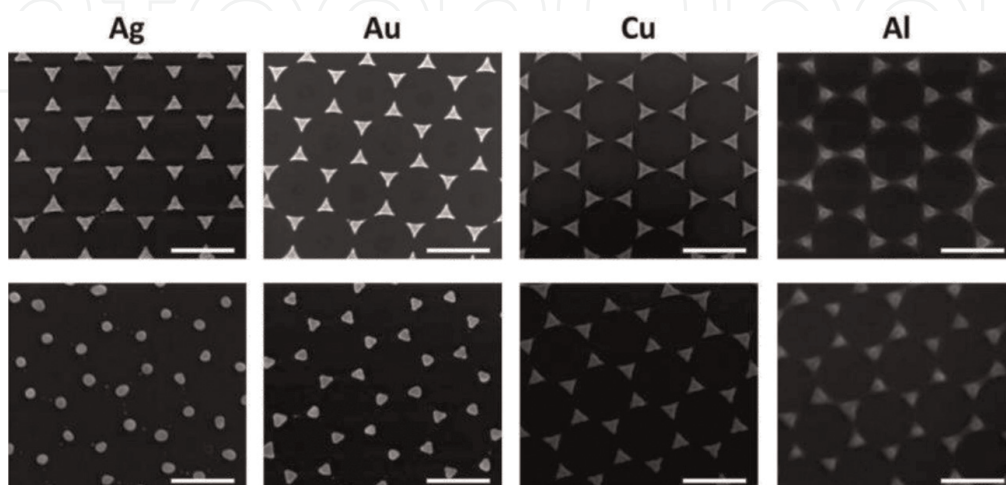

Figure 6.
SEM images of the nanostructures prepared by nanosphere lithography. Top row shows the structures as deposited and the bottom row after annealing at 500°C. The scale bar is 500 nm in all images [146].

Al, the change in shape is not so dramatic as they form a dense oxide layer *via* annealing thus preventing further shape changes (see **Figure 6**).

FEM simulations were performed using COMSOL 5.6 Wave Optic module [94]. The results are shown in **Figure 7**. There clearly is a blue shift of the resonant wavelength with increasing annealing temperature, that is, change of the shape for Ag, Au, and Cu arrays (**Figure 7a–c**), which is the main reason for the variation of the plasmonic resonance in this scenario. Additionally, the simulation for the Cu arrays is performed by adding a copper monoxide layer with the different thicknesses shown in **Figure 7c**. The results on the LSPR position support the hypothesis derived from the experimental results that annealing above 400°C produces thicker layers of copper oxide [146]. The electric field distribution (**Figure 7e**) reveals the position of the highest local enhancement for different copper oxide layer thicknesses.

The optical behavior of the metal NTs as a function of different annealing temperatures is a straightforward example of the flexibility in tuning the LSPR. Nanosphere lithography also allows other array structures to be fabricated, such as nanovoids [147] and "hedgehog-like" nanosphere arrays [148].

The metal nanotriangle structures have widely been used to study 2D materials, such as indium selenide (InSe) as shown in **Figure 8** [149]. One up to seven layers of InSe were deposited on arrays of plasmonic NTs composed of different metals. To
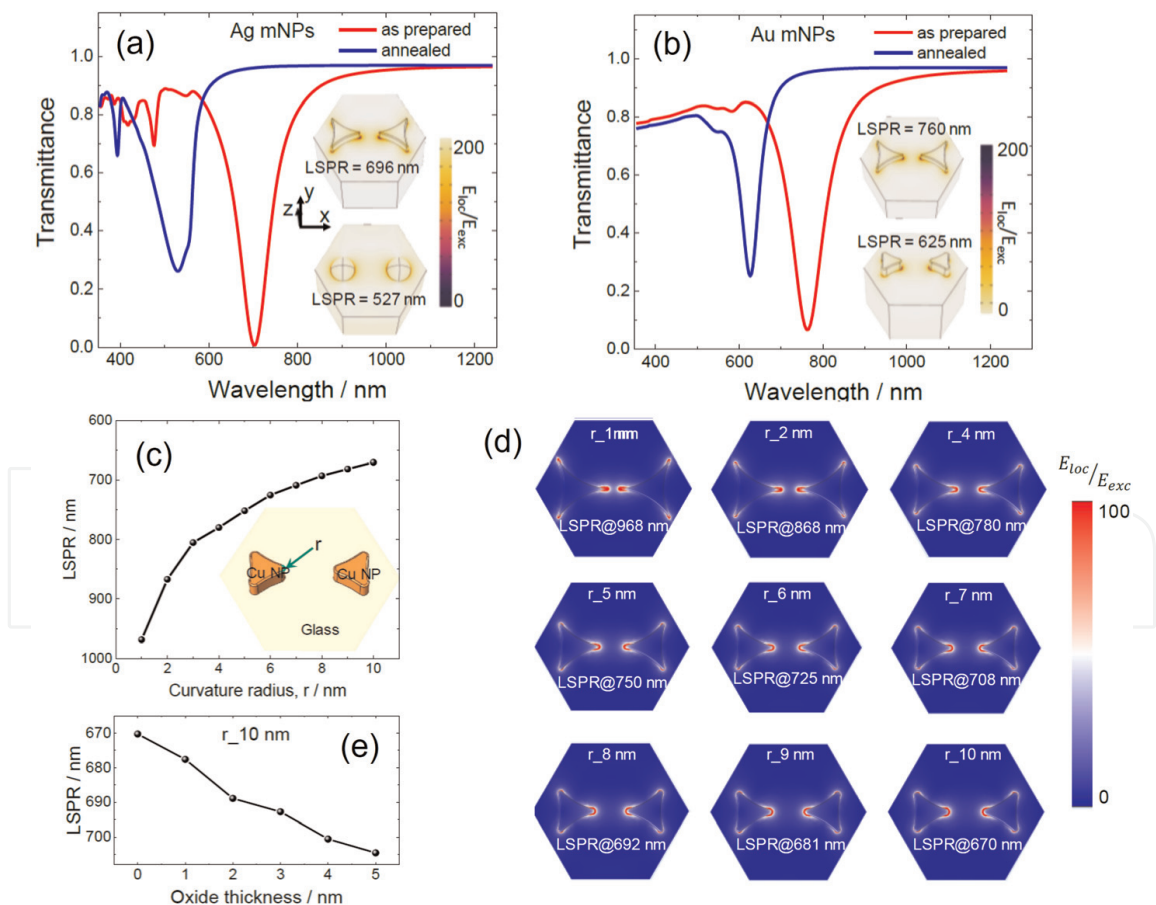

Figure 7.
Simulated transmission spectra and the electric field enhancement distribution at the LSPR position using geometries corresponding to as prepared and annealed Ag NPs (a) and Au NPs (b). Simulated LSPR positions vs. geometry change in a Cu array by changing the radius of the edge of the Cu triangles shown in the inset as a sketch mimicking the change of the geometry at the lower annealing temperature shown in (c) and the electric field enhancement distribution for Cu arrays at LSPR conditions shown in (d); (e) simulated LSPR for further increase of the oxide thickness mimicking the situation as annealing temperature further increases [146].
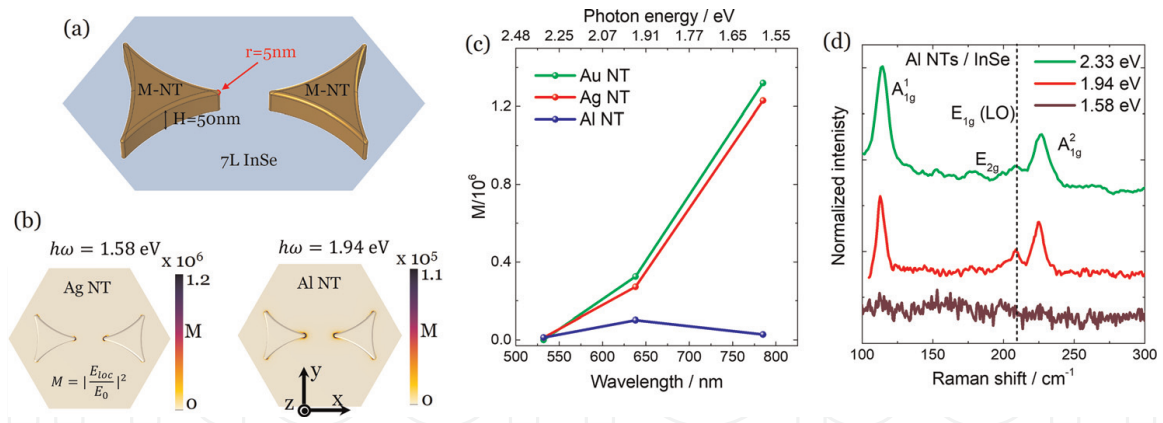
Figure 8.
FEM simulation of plasmonic coupling between InSe and metal nanotriangles (MNTs). (a) Sketch of the model used in the FEM simulation of InSe/metal NTs. (b) Simulated electric field intensity M distribution at two different wavelengths for Ag and Al NTs. (c) Absolute value of calculated maximum M at three different excitations. A similar plasmonic behavior is expected for Ag and Au NTs on InSe for three selected wavelengths, while InSe with Al NTs shows a maximum at 1.94-eV excitation. (d) Raman spectra of 7 L InSe with Al NTs acquired under three different wavelengths [149].

study the enhancement behavior, simulations were performed using the same conditions as in the experiment. The enhancement factor, M, is defined as the square of the local electric field strength enhancement. We can see dramatic enhancement for gold and silver nanotriangles (NTs) with excitation energy of 1.58 eV and a relatively large enhancement at 1.94 eV.

2.3.2 TERS

TERS is another important experimental technique based on plasmonic enhancement. In a typical TERS configuration, there is a metal tip that is used for scanning a substrate usually decorated with the analytes, for example, molecules or nanostructures. If the substrate is a metal, then such a configuration is called gap-mode TERS. One of the critical targets in this technique is to maximize the TERS signal enhancement and achieve very good spatial resolution in the nanometer range, well below the diffraction limit of light. Here, gold and silver are the two preferred materials for the plasmonic tips. For both materials, their LSPRs locate in the near infrared to visible range, where laser wavelengths are available to match the LSPR. Therefore, most of the experimental and simulation studies are performed using these two materials. Additionally, Au is normally the first choice because it is more chemically stable when exposed to air, enabling its use for longer periods of time, while Ag tends to form sulfides when exposed to air deteriorating the TERS performance [150].

2.4 Tip effects

A "sharp" metallic tip promises good spatial resolution. Therefore, as the most critical component in TERS, the tip is considered as a sharp "corner" of a metal rod. In the macroscopic world, a spark would form at the end of a long metal rod due to lightning bolt during a thunderstorm, and similarly in the nano-world, this effect also plays a vital role and contributes to the TERS signal enhancement. This was first explained in 1980 by Gersten and Nitzan [151] and then in 1982 by Wokaun [152] using the formulation of depolarization factors.

Considering a metallic ellipsoid with the major axis a and minor axis b with $a, b \ll \lambda$, so that the electrostatic approximation can be utilized. A uniform electric field E_L is applied along the major axis, and this leads to a uniform polarization density within such an ellipsoid [152].

$$P = \frac{1}{4\pi} \frac{\varepsilon_{ellip} - 1}{1 + (\varepsilon_{ellip} - 1)A_a} E_L \tag{15}$$

Then, the field at the tip of the ellipsoid can be written as:

$$E_{tip} = \frac{(1 - A_a)(\varepsilon_{ellip} - 1)}{1 + (\varepsilon_{ellip} - 1)A_a} E_L + E_L \tag{16}$$

where ε_{ellip} is the dielectric constant of the ellipsoid material and the A_a is the depolarization factor defined as:

$$A_a = \frac{ab^2}{2} \int_0^\infty \frac{ds}{(s + \alpha^2)R} \quad (\alpha = a, b) \tag{17}$$

with $R^2 = (s + a^2)(s + b^2)^2$. For a sphere, $A_a = \frac{1}{3}$ and for a prolate ellipsoid with ratio $a : b = 3 : 1$, $A_a = 0.1087$. The prominent effect that the depolarization factor gives is the shift of the plasmon resonance frequency, that is, when the denominators in Eq. (15) and Eq. (16) approach zero at a specific wavelength [152].

Now, we consider the nanoparticle dipole moment μ obtained by integrating Eq. (15) over the whole volume of the nanoparticle. This leads to $\mu = 4\pi ab^2 P/3$ [152].

The field of the nanoparticle is determined by the simple dipolar field of μ when at large distance. However, the situation changes when we look at the tip of the ellipsoid particle. A factor γ must be considered since the specific shape concentrates the field on the narrower parts of the structure. This phenomenon is called the lightning rod effect. We can then rewrite the Eq. (16) in a form of dipolar field $E_{dipolar} = 2\mu/a^3$ and the new E_{tip} is written as [152].

$$E_{tip} = \gamma E_{dipolar} + E_L \quad \text{where} \quad \gamma = \frac{3}{2}\left(\frac{a}{b}\right)^2 (1 - A_a) \tag{18}$$

We can see that for a sphere, $\gamma = 1$ with $a = b$ and therefore, $A_a = \frac{1}{3}$. For a prolate where $a : b = 3 : 1$, $\gamma = 12$. In the more extreme situation with a needle-like ellipsoid, we have $A_a \approx 0$ and $\gamma \approx \frac{3}{2}\left(\frac{a}{b}\right)^2$.

To calculate the total Raman enhancement, that is, an analyte molecule, for instance, is beneath the TERS tip, we consider the large Raman molecular moment that is induced by the intense local field at the ellipsoid and then the polarization of the ellipsoid induced by the molecular field. For simplicity, we can treat both the molecule and the ellipsoid as point dipoles. The molecular dipole field in turn polarizes the ellipsoid, giving an ellipsoid dipole at the Stokes frequency ω_s. This added-up molecular dipole is larger than the usual Raman molecular dipole by a factor of [152].

$$f = \frac{4}{9} \frac{\varepsilon(\omega_s) - 1}{[\varepsilon(\omega_s) - 1]A_a + 1} \times \frac{\varepsilon(\omega) - 1}{1 + [\varepsilon(\omega) - 1]A_a}\left(\frac{b^2}{a^2}\right)^2 \tag{19}$$

The Raman intensity enhancement is then given by $|f|^2$. Note that the depolarization factor A_a can be approximately written as follows when a/b is very large [152].

$$A_a \sim \left(\frac{b}{a}\right)^2 ln\left(\frac{a}{b}\right) \tag{20}$$

The lightning rod effect can be critical when simulating the electric field enhancement using geometrical simplifications. Therefore, for a tip geometry that is considered as a single sphere, the contribution to the signal enhancement due to the lightning rod effect is neglected.

The two most important aspects in TERS are the TERS enhancement factor (EF) and the spatial resolution. The TERS EF scales with $\left(\frac{E_{loc}}{E_{inc}}\right)^4$, where E_{loc} is the local electric field and E_{inc} is the incident electric field. The following classical theory provides a straightforward understanding [153]. To define the spatial resolution, the authors built a straightforward model for the TERS tip as shown in **Figure 9**. Here, the geometry of the tip can be approximated as a metal sphere, for which the solution was introduced in the previous section. The full-width at half maximum (FWHM) of the field distribution (mind that the real TERS spatial resolution is actually derived from the fourth power of the local electric field distribution) along the horizontal direction under the tip apex at a specific distance d from the tip apex [153]:

$$FWHM = 1.346(R + d) \tag{21}$$

The derived term indicates a supreme confined region of the local field, which is limited by the radius of the metal sphere or the curvature radius of a tip [154].

Simulations for an Ag tip with varying geometrical parameters were performed using COMSOL in ref. [155]. In this systematic simulation work, the simulated tip length, the tip radius, and the conical tip angle are varied [155]. As can be seen in **Figure 10**, there is a dramatic difference of the field enhancements between short and long tips, while a short, truncated tip can produce a better enhancement than a long one because of the excitation of the localized plasmon resonance. Regarding the tip radius, there is a significant improvement of the field enhancement observed when r decreases from 20 to 10 nm. Finally, the setting of the cone angle indeed influences the results but not as dramatic as the other two factors. Unfortunately, a direct proof of the spatial resolution derived in Eq. (20) cannot be found in the literature to our best knowledge.
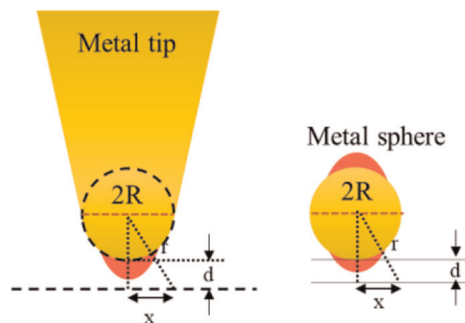

Figure 9.
Sketch of the geometric structure and local field distribution of a metal tip and its approximation as a single sphere [153].
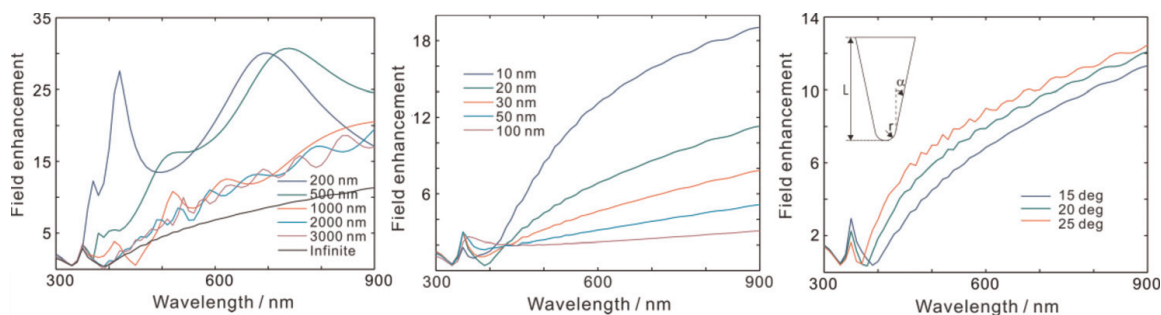
Figure 10.
a) Local electric field enhancement spectra for conical tips with different tip lengths l with the tip radius r = 20 nm and the tip cone angle α = 15°; b) local electric field enhancement spectra at the tip apex for different tip radii, and the tip length is kept as infinite and tip angle = 15°; c) local electric field enhancement spectra at the tip apex for different tip angles. The tip length is infinite and the tip radius r = 20 nm. Inset indicates the simulated tip geometry [155].

Due to the significance of the TERS tips, their fabrication became an important branch in the field of plasmonic [156, 157]. Different methods have been developed to produce metal TERS tips, such as electrochemical etching [158–160], electrodeposition [161, 162], and tip tailoring [163, 164]. Recently, Zhang developed an approach by concentrating the light *via* a waveguide and thus producing a low background hotspot at the tip apex [165].

Scanning electron microscope (SEM) images of commonly used tip geometries, namely of a) a sharp Au AFM tip, b) Au-coated spherical AFM tip and c) electrochemically deposited Au nanoparticle on a Pt AFM tip, are shown in **Figure 11** [166]. The related simulation work (shown in **Figure 12**) explained the experimental results.

Figures 11 and **12** show an example from tip fabrication to characterization and finally simulation. Here, the importance of the simulation is emphasized, and it not only helps to understand the optical response of the tip but can also help to design tips for specific resonance requirement. Thus, the simulation nowadays allows us from finding suitable experimental analytes to fulfilling instrument requirements and designing suitable experimental instruments for specific purposes.

2.5 Tip-substrate systems

Previously, it was demonstrated that a single metal tip alone can already enhance the electric field intensity in the vicinity of the tip apex due to its plasmonic resonance and the geometrical lightning rod effect. In a real TERS experiment, a metal substrate
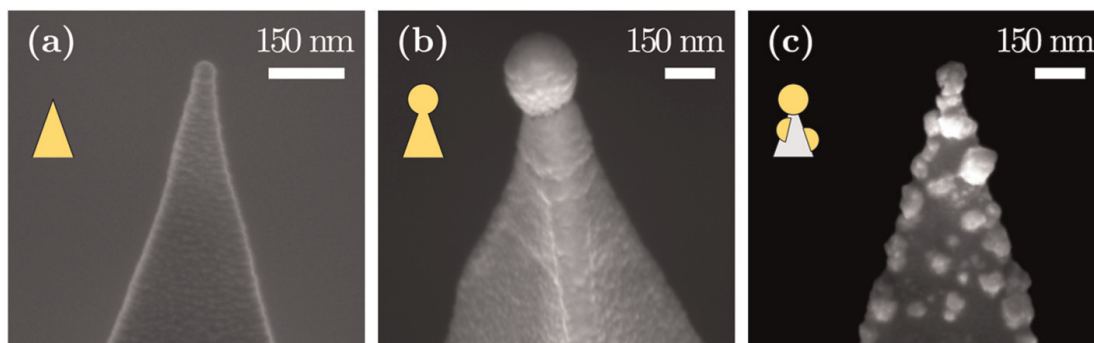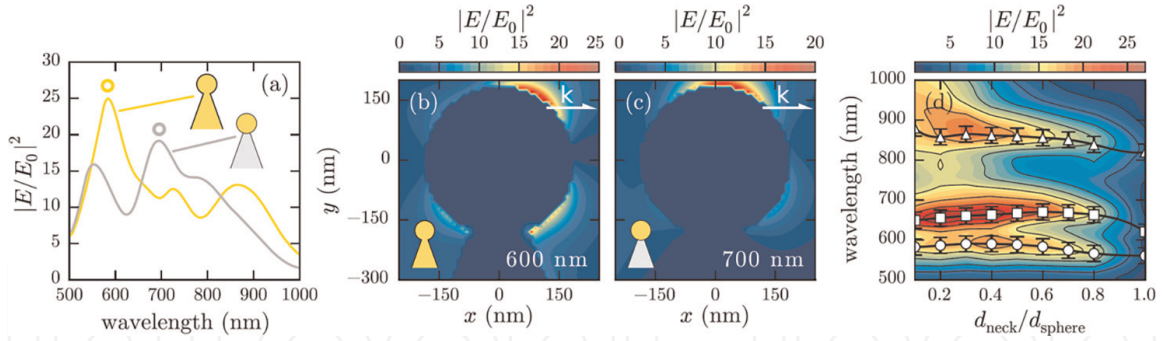

Figure 11.
SEM images of a) a sharp gold AFM tip; b) gold-coated spherical AFM tip, and c) electrochemically deposited gold nanoparticles on platinum AFM tip [166].

17

Figure 12.
a) Numerically simulated near-field spectra of spherical Au and AuNP-on-Pt tips with (b), (c) near-field maps of the main resonance as highlighted by circles in (a). Simulated tips have 300 nm spherical radii, 120 nm neck widths, 20° opening angles, and 1.88 μm lengths to best match the typical experimental tip geometries and avoid truncation artifacts. Tips are illuminated by plane waves oriented along the tip axis. (d) Interpolated field enhancement map with superimposed resonant wavelengths, as the neck width varies from a spherical to a sharp tip. Tips have a 250 nm apex diameter, 1.88 μm length, and 10° opening angle [166].

is usually present to further boost the signal. This type of configuration is called gap-mode TERS.

As shown in **Figure 13**, a gap-mode tip-substrate system can be considered as a dimer system composed of a metal sphere and its image dipole that is created in the metal film substrate [167]. Xu et al. gave a simple geometrical argument to estimate the local electric field in the gap of such dimer systems taking into consideration the drop in potential for the incident field E_{loc} [168].

The drop in potential between the two spheres shown in **Figure 13** (dashed circles) can be expressed as $\Delta V = |E_{loc}|d$, while the potential difference between these two sites in the absence of two metal spheres can be expressed as [153]:

$$\Delta V = |E_{inc}|(2R + d) \tag{22}$$

Since the two spheres can be considered as equipotential bodies, we can write

$$\Delta V = |E_{inc}|(2R + d) = |E_{loc}|d \tag{23}$$

In a specific geometry, where the radius of the sphere R and distance right beneath the tip apex d are fixed, the lateral offset of electric field from the center can be written as
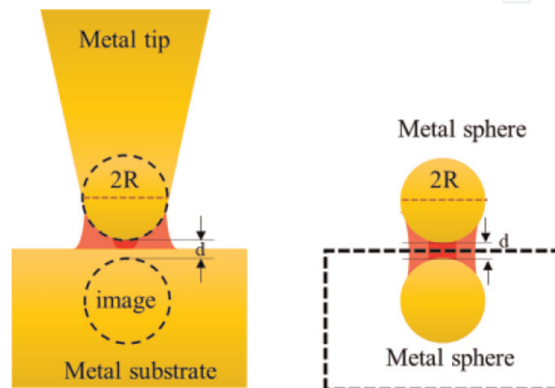
Figure 13.
Schematic presentation of metal tip-substrate structure and its approximation as a metal-sphere dimer [153].

$$|E_{loc}(x)| = \frac{\Delta V}{2R + d - 2\sqrt{R^2 - x^2}} \tag{24}$$

Therefore, the FWHM of the local field is given by $FWHM_{E_{loc}} = 2\sqrt{Rd}$ [153]. Considering the TERS intensity, which is proportional to the fourth power of the local electric field [169], we get

$$|E_{loc}(x)|^4 = \frac{\Delta V^4}{\left(2R + d - 2\sqrt{R^2 - x^2}\right)^4} \tag{25}$$

For a very small *d,* we can obtain the FWHM of the TERS intensity distribution as [170]:

$$FWHM_{TERS} = 2\sqrt{\left(\left(\sqrt[4]{2} - 1\right)Rd\right)} \approx 0.87\sqrt{Rd} \tag{26}$$

Many studies considered the easiest case of a substrate composed of a flat surface of a bulk material. The geometric parameters of the metal tip and the metal substrate with specific excitation wavelength using side illumination were evaluated numerically in ref. [169]. The study was performed using three-dimensional finite-difference time domain simulation (FDTD) and the effect of the presence of a substrate is demonstrated in **Figure 14**. Without a substrate, the electric field is enhanced by a factor $M = 20$ (see **Figure 14**, left), while it reaches $M = 189$ (see **Figure 14**, right) when there is a metal substrate.

Our own FEM simulation results on tip-substrate systems with various tip radii using the wave optics module in COMSOL 5.4 [93] are shown in **Figure 15**. To save the computational time, a two-dimensional model was built with a non-uniform mesh that guaranteed a very fine mesh grid element (less than 1 nm) in the region of the gap between the tip apex and the substrate [170].

To study the spectral dependence of each geometrical setting of various tip apex radii, a spectral sweep is performed from 500 nm to 800 nm. The results shown in
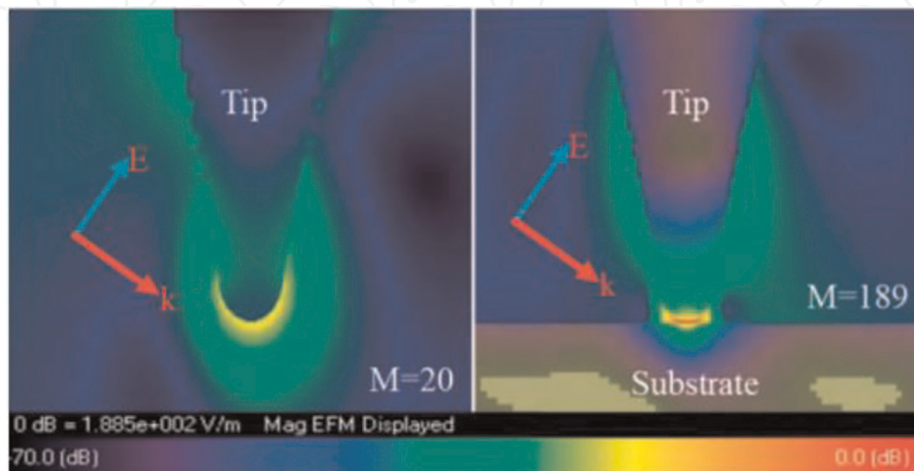

Figure 14.
FDTD simulations of the electric field distribution for a single Au tip (a), and a gold tip held at distance d = 2 nm from a gold substrate surface. The electric field E and wave vector k of the incoming light are displayed in the figures. M stands for the maximum enhancement [169].
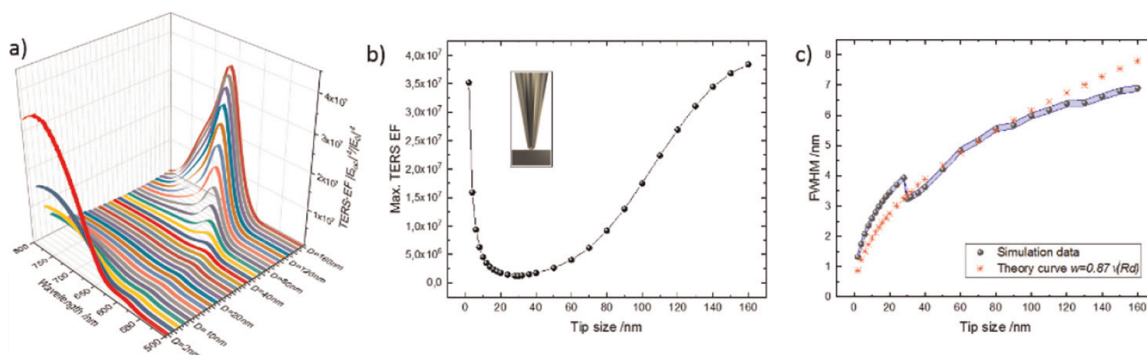
19

Figure 15.
*Simulation results of (a) the spectral dependence of the TERS EF as a function of tip diameter, (b) max. TERS EF, and (c) FWHM of the local TERS profile in the gap-mode TERS geometry as shown in the inset of **Figure 15b**. The simulated FWHM as a function of the tip diameter is compared with the FWHM profile derived from Eq. (26) (red asterisks in **Figure 15c**). The blue-shaded area presents the error bar of the FWHM [170].*

Figure 15 demonstrate a strong relation between the tip diameter and TERS enhancement factor with high spatial resolution, which is represented by the FWHM of the fourth power of the local field distribution beneath the tip apex. As the tip diameter increases from 30 nm to 160 nm, the increasing scattering cross section and the increasing radiative damping [171–173] both affect the enhancement factor, which increases and finally shows a saturation tendency.
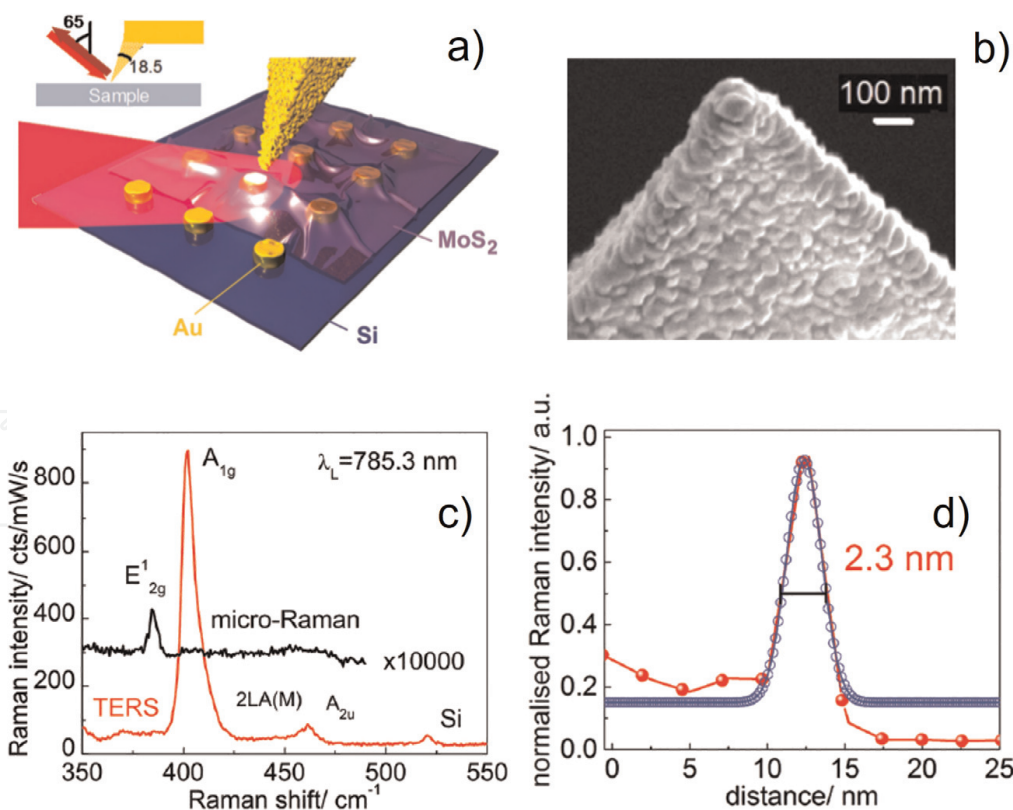

Figure 16.
a) Scheme of the TERS experiment. b) A magnified SEM image of a TERS tip revealing the formation of Au nanoclusters at and around the tip. C) A representative TERS spectrum of a MoS_2 monolayer on an Au nanocluster array in comparison with the spectrum excited by 785.3 nm light; d) Gaussian fit of an intensity profile obtained for a scan across the rim of a nanodisk. The spatial resolution of the TERS image is equal to the full width at half maximum (FWHM) of the fit (2.3 nm). Reproduced from ref. [174] with permission from the Royal Society of Chemistry.
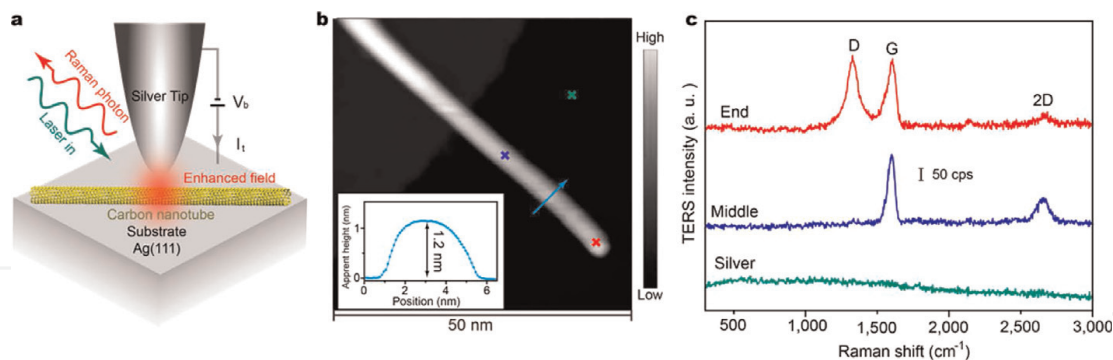
Figure 17.
a) Schematic illustration of the STM-TERS experiments. b) STM topography of an isolated CNT on Ag (111) (1 V, 10 pA). Inset: Line profile of the CNT along the blue arrow line. c) Apparent height profile and TERS intensity profiles along the long end of a carbon nanotube [175].

Utilizing gap-mode TERS, Rahaman et al. performed TERS studies of MoS_2 layers on gold nanodisk arrays under the ambient conditions. They used a side illuminated AFM-TERS (**Figure 16a**) experimental configuration with a gold-coated Si AFM tip. The SEM image of the tip apex is shown in **Figure 16b**. The TERS enhancement factor was calculated using the A_{1g} mode of MoS_2 and it reached 5.6×10^8 (**Figure 16c**), while a spatial resolution of 2.3 nm was achieved (**Figure 16d**) [174].

STM-based TERS, on the other hand, can produce even better spatial resolution due to the sharpness of the STM tips and the controlled experimental environment. Liao used a STM-TERS system as sketched in **Figure 17a** on a carbon nanotube placed on an Ag (111) substrate. A STM topography image can be seen in **Figure 17b** [175]. They claimed a spatial resolution of 0.7 nm (**Figure 17c**) with a TERS EF of approximately 10^8.

3. Conclusions

The geometry of plasmonic structures plays a key role and is an essential property of a plasmonic system. For SERS systems composed of metal nanoparticles without a supporting substrate or on a non-metal substrate, a single particle may not create significant enhancement, while their agglomeration demonstrates a much more enhanced signal both theoretically and experimentally. This is due to the existence of the hotspots that are created in small gap between the single elements. For a gap-mode SERS system, a good overall enhancement factor can be expected as the hotspots are created between the particle and the substrate, and/or between the plasmonic particles themselves. Finally, metal nanostructure arrays provide a versatile tool in the SERS catalog. Their optical resonance behavior can be tuned *via* changing their shapes using different approaches. For TERS systems, the lightening rod effect, which is induced by any geometric anisotropy, and the LSPR, which is influenced by the tip geometry and material, are the two most critical experimental and theoretical parameters, while the real experiment is usually performed in the so-called gap-mode TERS using metal substrates with metal tips. Despite the flexibility of the simulation tools addressing TERS experiments, the modeling of such experiments is still challenging due to the difficulties providing different and precise dimensions of active tips and

substrates. Nevertheless, the support of experimental results by the simulations or the planning of any SERS or TERS experiment using simulation tools is of major importance toward the understanding of the physics of plasmonic systems and in providing a better control over the measurement itself.

Acknowledgements

Conflict of interest

The authors declare no conflict of interest.

Author details

Lu He*, Dietrich R.T. Zahn and Teresa I. Madeira
Semiconductor Physics, Chemnitz University of Technology, Chemnitz, Germany

*Address all correspondence to: lu.he@physik.tu-chemnitz.de

IntechOpen

References

[1] Fleischmann M, Hendra PJ, McQuillan AJ. Raman spectra of pyridine adsorbed at a silver electrode. Chemical Physics Letters. 1974;**26**(2):163-166. DOI: 10.1016/0009-2614(74)85388-1

[2] Albrecht MG, Creighton JA. Anomalously intense Raman spectra of pyridine at a silver electrode. Journal of the American Chemical Society. 1977;**99**(15): 5215-5217. DOI: 10.1021/ja00457a071

[3] Jeanmaire DL, van Duyne RP. Surface Raman spectroelectrochemistry. Journal of Electroanalytical Chemistry and Interfacial Electrochemistry. 1977;**84**(1): 1-20. DOI: 10.1016/S0022-0728(77)80224-6

[4] Wood TH, Zwemer DA, Shank CV, Rowe JE. The dependence of surface-enhanced Raman scattering on surface preparation: Evidence for an electromagnetic mechanism. Chemical Physics Letters. 1981;**82**(1):5-8. DOI: 10.1016/0009-2614(81)85095-6

[5] Moskovits M. Surface roughness and the enhanced intensity of Raman scattering by molecules adsorbed on metals. The Journal of Chemical Physics. 1978;**69**(9): 4159-4161. DOI: 10.1063/1.437095

[6] Creighton JA, Albrecht MG, Hester RE, Matthew J. The dependence of the intensity of Raman bands of pyridine at a silver electrode on the wavelength of excitation. Chemical Physics Letters. 1978;**55**(1):55-58. DOI: 10.1016/0009-2614(78)85131-8

[7] Goad DGW, Moskovits M. Colloidal metal in aluminum-oxide. Journal of Applied Physics. 1978;**49**(5):2929-2934. DOI: 10.1063/1.325153

[8] Phillip OLK. Optical properties of individual nano-sized gold particle pairs.

In: Mie-Scattering, Fluorescence, and Raman-Scattering. Germany: TU Dresden

[9] Kolwas K, Derkachova A. Impact of the Interband transitions in gold and silver on the dynamics of propagating and localized surface Plasmons. Nanomaterials (Basel). 2020;**10**(7):1411. DOI: 10.3390/nano10071411

[10] Shrivastav AM, Cvelbar U, Abdulhalim I. A comprehensive review on plasmonic-based biosensors used in viral diagnostics. Communications Biology. 2021;**4**(1):70. DOI: 10.1038/s42003-020-01615-8

[11] Cortés E, Xie W, Cambiasso J, et al. Plasmonic hot electron transport drives nano-localized chemistry. Nature Communications. 2017;**8**:14880. DOI: 10.1038/ncomms14880

[12] Flick J, Rivera N, Narang P. Strong light-matter coupling in quantum chemistry and quantum photonics. Nano. 2018;**7**(9):1479-1501. DOI: 10.1515/nanoph-2018-0067

[13] Oksenberg E, Shlesinger I, Xomalis A, et al. Energy-resolved plasmonic chemistry in individual nanoreactors. Nature Nanotechnology. 2021;**16**(12):1378-1385. DOI: 10.1038/s41565-021-00973-6

[14] Schürmann R, Nagel A, Juergensen S, et al. Microscopic understanding of reaction rates observed in Plasmon chemistry of nanoparticle-ligand systems. The Journal of Physical Chemistry. C, Nanomaterials and Interfaces. 2022;**126**(11):5333-5342. DOI: 10.1021/acs.jpcc.2c00278

[15] Davis TJ, Gómez DE, Roberts A. Plasmonic circuits for manipulating

optical information. Nano. 2016;**6**(3): 543-559. DOI: 10.1515/nanoph-2016-0131

[16] Huang Y, Fang Y, Zhang Z, Zhu L, Sun M. Nanowire-supported plasmonic waveguide for remote excitation of surface-enhanced Raman scattering. Light: Science & Applications. 2014;**3**(8):e199-e199. DOI: 10.1038/lsa.2014.80

[17] Aalizadeh M, Khavasi A, Serebryannikov AE, Vandenbosch GAE, Ozbay E. A route to unusually broadband Plasmonic absorption spanning from visible to mid-infrared. Plasmonics. 2019;**14**(5):1269-1281. DOI: 10.1007/s11468-019-00916-x

[18] Tong J, Zhou W, Qu Y, Xu Z, Huang Z, Zhang DH. Surface plasmon induced direct detection of long wavelength photons. Nature Communications. 2017;**8**(1):1660. DOI: 10.1038/s41467-017-01828-2

[19] Liu A, Peng J, Li G. Characterizing penetration depths of multi-wavelength surface plasmon resonance sensor using silica beads. Applied Physics Letters. 2014;**104**(21):211103. DOI: 10.1063/1.4879830

[20] Ai B, Fan Z, Wong ZJ. Plasmonic-perovskite solar cells, light emitters, and sensors. Microsystems & Nanoengineering. 2022;**8**:5. DOI: 10.1038/s41378-021-00334-2

[21] Aubry A, Lei DY, Fernández-Domínguez AI, Sonnefraud Y, Maier SA, Pendry JB. Plasmonic light-harvesting devices over the whole visible spectrum. Nano Letters. 2010;**10**(7):2574-2579. DOI: 10.1021/nl101235d

[22] Mie G. Beiträge zur Optik trüber Medien, speziell kolloidaler Metallösungen. Ann. Phys. 1908;**330**(3): 377-445. DOI: 10.1002/andp.19083300302

[23] Gersten JI, Weitz DA, Gramila TJ, Genack AZ. Inelastic Mie scattering from rough metal surfaces: Theory and experiment. Physical Review B. 1980;**22**(10):4562-4571. DOI: 10.1103/PhysRevB.22.4562

[24] Gersten JI. Rayleigh, Mie, and Raman scattering by molecules adsorbed on rough surfaces. The Journal of Chemical Physics. 1980;**72**(10): 5780-5781. DOI: 10.1063/1.439003

[25] Tiggesbäumker K, Meiwes-Broer L. Blue shift of the Mie plasma frequency in Ag clusters and particles. Physical Review A. 1993;**48**(3):R1749-R1752. DOI: 10.1103/physreva.48.r1749

[26] Papoff F, Hourahine B. Geometrical Mie theory for resonances in nanoparticles of any shape. Optics Express. 2011;**19**(22):21432-21444. DOI: 10.1364/OE.19.021432

[27] You C, Nellikka AC, de Leon I, Magaña-Loaiza OS. Multiparticle quantum plasmonics. Nano. 2020;**9**(6): 1243-1269. DOI: 10.1515/nanoph-2019-0517

[28] Jamshidi Z, Asadi-Aghbolaghi N, Morad R, et al. Comparing the nature of quantum plasmonic excitations for closely spaced silver and gold dimers. The Journal of Chemical Physics. 2022;**156**(7):74102. DOI: 10.1063/5.0079258

[29] Xiang H, Zu J, Jiang H, Xu L, Lu G, Zhang X. Understanding quantum Plasmonic enhancement in Nanorod dimers from time-dependent orbital-free density functional theory. Journal of Physical Chemistry C. 2022;**126**(10): 5046-5054. DOI: 10.1021/acs.jpcc.2c00105

[30] Maier SA. Plasmonics: Fundamentals and Applications. New York: Springer; 2007

[31] Esteban R, Borisov AG, Nordlander P, Aizpurua J. Bridging quantum and classical plasmonics with a quantum-corrected model. Nature Communications. 2012;**3**:825. DOI: 10.1038/ncomms1806

[32] Tame MS, McEnery KR, Özdemir ŞK, Lee J, Maier SA, Kim MS. Quantum plasmonics. Nature Physics. 2013;**9**(6): 329-340. DOI: 10.1038/nphys2615

[33] Varas A, García-González P, Feist J, García-Vidal FJ, Rubio A. Quantum plasmonics: From jellium models to ab initio calculations. Nano. 2016;**5**(3): 409-426. DOI: 10.1515/nanoph-2015-0141

[34] Zhu W, Esteban R, Borisov AG, et al. Quantum mechanical effects in plasmonic structures with subnanometre gaps. Nature Communications. 2016;**7**: 11495. DOI: 10.1038/ncomms11495

[35] Da X, Xiong X, Wu L, et al. Quantum plasmonics: New opportunity in fundamental and applied photonics. Advances in Optics and Photonics. 2018; **10**(4):703. DOI: 10.1364/ AOP.10.000703

[36] Fiederling K, Abasifard M, Richter M, Deckert V, Gräfe S, Kupfer S. The chemical effect goes resonant - a full quantum mechanical approach on TERS. Nanoscale. 2020;**12**(11):6346-6359. DOI: 10.1039/c9nr09814c

[37] Lovász B, Sándor P, Kiss G-Z, et al. Nonadiabatic Nano-optical tunneling of photoelectrons in Plasmonic Near-fields. Nano Letters. 2022;**22**(6):2303-2308. DOI: 10.1021/acs.nanolett.1c04651

[38] Bohren CF, Huffman DR. Absorption and Scattering of Light by Small Particles. New York, Chichester: Wiley; 1993 (1998[printing])

[39] Jensen T, Kelly L, Lazarides A, Schatz GC. Electrodynamics of Noble metal nanoparticles and nanoparticle clusters. Journal of Cluster Science. 1999; **10**(2):295-317. DOI: 10.1023/A: 1021977613319

[40] Fan X, Zheng W, Singh DJ. Light scattering and surface plasmons on small spherical particles. Light: Science & Applications. 2014;**3**(6):e179-e179. DOI: 10.1038/lsa.2014.60

[41] Coronado EA, Schatz GC. Surface plasmon broadening for arbitrary shape nanoparticles: A geometrical probability approach. The Journal of Chemical Physics. 2003;**119**(7):3926-3934. DOI: 10.1063/1.1587686

[42] Kelly KL, Coronado E, Zhao LL, Schatz GC. The optical properties of metal nanoparticles: The influence of size, shape, and dielectric environment. The Journal of Physical Chemistry. B. 2003;**107**(3):668-677. DOI: 10.1021/ jp026731y

[43] Diaz HRR, Esquivel-Sirvent R, Noguez C. Plasmonic response of nested nanoparticles with arbitrary geometry. Journal of Physical Chemistry C. 2016; **120**(4):2349-2354. DOI: 10.1021/acs. jpcc.5b10109

[44] Schnitzer O, Giannini V, Maier SA, Craster RV. Surface plasmon resonances of arbitrarily shaped nanometallic structures in the small-screening-length limit. Proceedings. Mathematical, Physical, and Engineering Sciences. 2016;**472**(2191):20160258. DOI: 10.1098/ rspa.2016.0258

[45] Kamandar Dezfouli M, Tserkezis C, Mortensen NA, Hughes S. Nonlocal quasinormal modes for arbitrarily

shaped three-dimensional plasmonic resonators. Optica. 2017;**4**(12):1503. DOI: 10.1364/OPTICA.4.001503

[46] Santiago EY, Besteiro LV, Kong X-T, Correa-Duarte MA, Wang Z, Govorov AO. Efficiency of hot-electron generation in Plasmonic nanocrystals with complex shapes: Surface-induced scattering, hot spots, and Interband transitions. ACS Photonics. 2020;**7**(10): 2807-2824. DOI: 10.1021/acsphotonics.0c01065

[47] Chung HY, Guo GY, Chiang H-P, Tsai DP, Leung PT. Accurate description of the optical response of a multilayered spherical system in the long wavelength approximation. Physical Review B. 2010; **82**(16):165440. DOI: 10.1103/PhysRevB.82.165440

[48] Rasskazov IL, Zakomirnyi VI, Utyushev AD, Carney PS, Moroz A. Remarkable predictive power of the modified long wavelength approximation. Journal of Physical Chemistry C. 2021;**125**(3):1963-1971. DOI: 10.1021/acs.jpcc.0c09774

[49] Chung HY, Leung PT, Tsai DP. Modified long wavelength approximation for the optical response of a graded-index Plasmonic nanoparticle. Plasmonics. 2012;**7**(1): 13-18. DOI: 10.1007/s11468-011-9269-5

[50] Fornasiero D, Grieser F. Analysis of the visible absorption and SERS excitation spectra of silver sols. The Journal of Chemical Physics. 1987;**87**(5): 3213-3217. DOI: 10.1063/1.453009

[51] Kolwas K, Derkachova A. Plasmonic abilities of gold and silver spherical nanoantennas in terms of size dependent multipolar resonance frequencies and plasmon damping rates. Opto-Electronics Review. 2010;**18**(4):429-437. DOI: 10.2478/s11772-010-0043-6

[52] Lee Y-J, Schade NB, Sun L, et al. Ultrasmooth, highly spherical monocrystalline gold particles for precision plasmonics. ACS Nano. 2013;**7**(12): 11064-11070. DOI: 10.1021/nn404765w

[53] Link S, El-Sayed MA. Spectral properties and relaxation dynamics of surface Plasmon electronic oscillations in gold and silver Nanodots and Nanorods. The Journal of Physical Chemistry. B. 1999;**103**(40):8410-8426. DOI: 10.1021/jp9917648

[54] Lermé J. Size evolution of the surface Plasmon resonance damping in silver nanoparticles: Confinement and dielectric effects. Journal of Physical Chemistry C. 2011;**115**(29):14098-14110. DOI: 10.1021/jp203481m

[55] Charlé K-P, König L, Nepijko S, Rabin I, Schulze W. The surface Plasmon resonance of free and embedded Ag-clusters in the size range 1,5 nm < D < 30 nm. Crystal Research and Technology. 1998;**33**(7–8):1085-1096. DOI: 10.1002/(SICI)1521-4079(199810) 33:7/8<1085::AID-CRAT1085>3.0.CO; 2-A

[56] Kreibig U, Vollmer M. Theoretical considerations. In: Toennies JP, Gonser U, Osgood RM, et al., editors. Optical Properties of Metal Clusters. Berlin, Heidelberg: Springer Berlin Heidelberg; 1995. pp. 13-201

[57] Dhara AK, Ghosh SK. Density-functional theory for time-dependent systems. Physical Review A. 1987;**35**:442

[58] Yabana B. Time-dependent local-density approximation in real time. Physical Review B: Condensed Matter. 1996;**54**(7):4484-4487. DOI: 10.1103/physrevb.54.4484

[59] Sholl DS, Steckel JA. In: Sholl JA, Steckel., editors. Density Functional

Theory: A Practical Introduction/
David S. Hoboken, N.J: Wiley; 2009

[60] Prodan E, Radloff C, Halas NJ,
Nordlander P. A hybridization model for
the plasmon response of complex
nanostructures. Science. 2003;
302(5644):419-422. DOI: 10.1126/
science.1089171

[61] Nordlander P, Oubre C, Prodan E,
Li K, Stockman MI. Plasmon
hybridization in nanoparticle dimers.
Nano Letters. 2004;**4**(5):899-903.
DOI: 10.1021/nl049681c

[62] Prodan E, Nordlander P. Structural
Tunability of the Plasmon resonances in
metallic Nanoshells. Nano Letters.
2003;**3**(4):543-547. DOI: 10.1021/
nl034030m

[63] Oubre C, Nordlander PJ. Finite
difference time-domain studies of
optical properties of nanoshell
structures. In: Proceedings SPIE 5221.
Plasmonics: Metallic Nanostructures and
Their Optical Properties. 2003. DOI:
10.1117/12.511664. [28 October 2003]

[64] Mohsin ASM, Salim MB. Probing the
Plasmon coupling, quantum yield, and
effects of tip geometry of gold
nanoparticle using analytical models and
FDTD simulation. IEEE Photonics
Journal. 2018;**10**(3):1-10. DOI: 10.1109/
JPHOT.2018.2825435

[65] Benz F, Nijs B de, Tserkezis C, et al.
Generalized circuit model for coupled
plasmonic systems. Optics Express 2015;
23(26):33255–33269 [DOI: 10.1364/
OE.23.033255]

[66] Jeong H-H, Adams MC, Günther J-P,
et al. Arrays of Plasmonic nanoparticle
dimers with defined Nanogap spacers.
ACS Nano. 2019;**13**(10):11453-11459.
DOI: 10.1021/acsnano.9b04938

[67] Arbuz A, Sultangaziyev A,
Rapikov A, Kunushpayeva Z, Bukasov R.
How gap distance between gold
nanoparticles in dimers and trimers on
metallic and non-metallic SERS substrates
can impact signal enhancement.
Nanoscale Advances. 2021;**4**(1):268-280.
DOI: 10.1039/D1NA00114K

[68] Jain PK, Huang W, El-Sayed MA. On
the universal scaling behavior of the
distance decay of Plasmon coupling in
metal nanoparticle pairs: A Plasmon
ruler equation. Nano Letters. 2007;**7**(7):
2080-2088. DOI: 10.1021/nl071008a

[69] Aćimović SS, Kreuzer MP,
González MU, Quidant R. Plasmon near-
field coupling in metal dimers as a step
toward single-molecule sensing. ACS
Nano. 2009;**3**(5):1231-1237.
DOI: 10.1021/nn900102j

[70] Funston AM, Novo C, Davis TJ,
Mulvaney P. Plasmon coupling of gold
nanorods at short distances and in
different geometries. Nano Letters.
2009;**9**(4):1651-1658. DOI: 10.1021/
nl900034v

[71] Masango SS, Hackler RA, Large N,
et al. High-resolution distance
dependence study of surface-enhanced
Raman scattering enabled by atomic
layer deposition. Nano Letters. 2016;
16(7):4251-4259. DOI: 10.1021/acs.
nanolett.6b01276

[72] Song J-H, Raza S, van de Groep J,
et al. Nanoelectromechanical modulation
of a strongly-coupled plasmonic dimer.
Nature Communications. 2021;**12**(1):48.
DOI: 10.1038/s41467-020-20273-2

[73] Wang X, Huang S-C, Hu S, Yan S,
Ren B. Fundamental understanding and
applications of plasmon-enhanced
Raman spectroscopy. Nature Reviews
Physics. 2020;**2**(5):253-271.
DOI: 10.1038/s42254-020-0171-y

[74] Kudelski A, Wojtysiak S. Silica-covered silver and gold Nanoresonators for Raman analysis of surfaces of various materials. Journal of Physical Chemistry C. 2012;**116**(30):16167-16174. DOI: 10.1021/jp304409x

[75] Sivanesan A, Kozuch J, Ly HK, Kalaivani G, Fischer A, Weidinger IM. Tailored silica coated Ag nanoparticles for non-invasive surface enhanced Raman spectroscopy of biomolecular targets. RSC Advances. 2012;**2**(3): 805-808. DOI: 10.1039/C1RA00781E

[76] Kołątaj K, Krajczewski J, Kudelski A. Silver nanoparticles with many sharp apexes and edges as efficient Nanoresonators for Shell-isolated nanoparticle-enhanced Raman spectroscopy. Journal of Physical Chemistry C. 2017;**121**(22):12383-12391. DOI: 10.1021/acs.jpcc.7b02695

[77] Barbillon G. Applications of Shell-isolated nanoparticle-enhanced Raman spectroscopy. Photonics. 2021;**8**(2):46. DOI: 10.3390/photonics8020046

[78] Avakyan LA, Heinz M, Skidanenko AV, et al. Insight on agglomerates of gold nanoparticles in glass based on surface plasmon resonance spectrum: Study by multi-spheres T-matrix method. Journal of Physics. Condensed Matter. 2018;**30**(4): 45901. DOI: 10.1088/1361-648X/aa9fcc

[79] Pawlak M, Bagiński M, Llombart P, et al. Tuneable helices of plasmonic nanoparticles using liquid crystal templates: Molecular dynamics investigation of an unusual odd-even effect in liquid crystalline dimers. Chemical Communications (Camb). 2022;**58**(53):7364-7367. DOI: 10.1039/d2cc00560c

[80] Nečada M, Törmä P. Multiple-scattering T-matrix simulations for nanophotonics: Symmetries and periodic lattices. CiCP. 2021;**30**(2):357-395. DOI: 10.4208/cicp.OA-2020-0136

[81] Khlebtsov NG. T-matrix method in plasmonics: An overview. Journal of Quantitative Spectroscopy and Radiative Transfer. 2013;**123**:184-217. DOI: 10.1016/j.jqsrt.2012.12.027

[82] Demchuk A, Bolesta I, Kushnir O, Kolych I. The computational studies of Plasmon interaction. Nanoscale Research Letters. 2017;**12**(1):273. DOI: 10.1186/s11671-017-2050-8

[83] Yurkin MA, Hoekstra AG. The discrete dipole approximation: An overview and recent developments. Journal of Quantitative Spectroscopy and Radiative Transfer. 2007;**106**(1–3): 558-589. DOI: 10.1016/j.jqsrt.2007.01.034

[84] Burger S, Zschiedrich L, Pomplun J, Schmidt F. Finite element method for accurate 3D simulation of plasmonic waveguides, SPIE OPTO, 2010, San Francisco, California, United States. 2010;**7604**:76040F. [DOI:10.1117/12.841995]

[85] Downes A, Salter D, Elfick A. Simulations of tip-enhanced optical microscopy reveal atomic resolution. Journal of Microscopy. 2008;**229**(Pt 2): 184-188. DOI: 10.1111/j.1365-2818.2008.01884.x

[86] Remcom. FDTD Method for Electromagnetic Simulation — Remcom. 2022. Available from: https://www.remcom.com/electromagnetic-simulation-numerical-methods/fdtd-method-simulation-software [Accessed: August 11, 2022]

[87] Smajic J, Hafner C, Raguin L, Tavzarashvili K, Mishrikey M. Comparison of numerical methods for

the analysis of Plasmonic structures. Journal of Computational and Theoretical Nanoscience. 2009; **6**(3):763-774. DOI: 10.1166/jctn.2009. 1107

[88] Liu Y-C, Chang K, Fwu J, Shih L. Performance comparison between FDTD and FEM for the simulation of plasmonic waveguide operating at optical communication frequency. 2013 USNC-URSI Radio Science Meeting (Joint with AP-S Symposium). 2013. pp. 184-184, DOI: 10.1109/USNC-URSI.2013.6715490

[89] Parsons J, Burrows CP, Sambles JR, Barnes WL. A comparison of techniques used to simulate the scattering of electromagnetic radiation by metallic nanostructures. Journal of Modern Optics. 2010;**57**(5):356-365. DOI: 10.1080/09500341003628702

[90] Rapp BE, editor. Chapter 32—Finite Element Method[J]. Microfluidics: Modelling, Mechanics and Mathematics; Micro and Nano Technologies. 2017:655-678

[91] Lesina AC, Vaccari A, Berini P, Ramunno L. On the convergence and accuracy of the FDTD method for nanoplasmonics. Optics Express. 2015; **23**(8):10481-10497. DOI: 10.1364/OE.23.010481

[92] Gonçalves MR. Plasmonic nanoparticles: Fabrication, simulation and experiments. Journal of Physics D: Applied Physics. 2014;**47**(21):213001. DOI: 10.1088/0022-3727/47/21/213001

[93] COMSOL Multiphysics. Available from: https://www.comsol.com/

[94] Wave Optics Module User's Guide, COMSOL Multiphysics® v. 5.6. COMSOL AB, Stockholm, Sweden. 2021

[95] Zhang Y, Walkenfort B, Yoon JH, Schlücker S, Xie W. Gold and silver nanoparticle monomers are non-SERS-active: A negative experimental study with silica-encapsulated Raman-reporter-coated metal colloids. Physical Chemistry Chemical Physics. 2015; **17**(33):21120-21126. DOI: 10.1039/c4cp05073h

[96] Majić MRA, Auguié B, Le Ru EC. Comparison of dynamic corrections to the quasistatic polarizability and optical properties of small spheroidal particles. The Journal of Chemical Physics. 2022; **156**(10):104110. DOI: 10.1063/5.0085687

[97] Majic M, Pratley L, Schebarchov D, Somerville WRC, Auguié B, Le Ru EC. Approximate T matrix and optical properties of spheroidal particles to third order with respect to size parameter. Physical Review A. 2019;**99**(1):013853. DOI: 10.1103/PhysRevA.99.013853

[98] Takeuchi T, Noda M, Yabana K. Operation of quantum Plasmonic Metasurfaces using electron transport through subnanometer gaps. ACS Photonics. 2019;**6**(10):2517-2522. DOI: 10.1021/acsphotonics.9b00889

[99] Zuloaga J, Prodan E, Nordlander P. Quantum description of the plasmon resonances of a nanoparticle dimer. Nano Letters. 2009;**9**(2):887-891. DOI: 10.1021/nl803811g

[100] Barbry M, Koval P, Marchesin F, et al. Atomistic near-field nanoplasmonics: Reaching atomic-scale resolution in nanooptics. Nano Letters. 2015;**15**(5):3410-3419. DOI: 10.1021/acs.nanolett.5b00759

[101] Mao L, Li Z, Wu B, Xu H. Effects of quantum tunneling in metal nanogap on surface-enhanced Raman scattering. Applied Physics Letters. 2009;**94**(24): 243102. DOI: 10.1063/1.3155157

[102] Savage KJ, Hawkeye MM, Esteban R, Borisov AG, Aizpurua J, Baumberg JJ. Revealing the quantum regime in tunnelling plasmonics. Nature. 2012;**491**(7425):574-577. DOI: 10.1038/nature11653

[103] Scholl JA, García-Etxarri A, Koh AL, Dionne JA. Observation of quantum tunneling between two plasmonic nanoparticles. Nano Letters. 2013;**13**(2):564-569. DOI: 10.1021/nl304078v

[104] Scholl JA, Garcia-Etxarri A, Aguirregabiria G, et al. Evolution of Plasmonic Metamolecule modes in the quantum tunneling regime. ACS Nano. 2016;**10**(1):1346-1354. DOI: 10.1021/acsnano.5b06738

[105] Liu Z, Zhang F, Yang Z, et al. Gold mesoparticles with precisely controlled surface topographies for single-particle surface-enhanced Raman spectroscopy. Journal of Materials Chemistry C. 2013;**1**(35):5567. DOI: 10.1039/c3tc30824c

[106] Minati L, Benetti F, Chiappini A, Speranza G. One-step synthesis of star-shaped gold nanoparticles. Colloids and Surfaces A: Physicochemical and Engineering Aspects. 2014;**441**:623-628. DOI: 10.1016/j.colsurfa.2013.10.025

[107] Giannini V, Rodríguez-Oliveros R, Sánchez-Gil JA. Surface Plasmon resonances of metallic Nanostars/Nanoflowers for surface-enhanced Raman scattering. Plasmonics. 2010;**5**(1):99-104. DOI: 10.1007/s11468-009-9121-3

[108] Mazzucco S, Stéphan O, Colliex C, et al. Spatially resolved measurements of plasmonic eigenstates in complex-shaped, asymmetric nanoparticles: Gold nanostars. European Physical Journal Applied Physics. 2011;**54**(3):33512. DOI: 10.1051/epjap/2011100443

[109] Garcia-Leis A, Torreggiani A, Garcia-Ramos JV, Sanchez-Cortes S. Hollow Au/Ag nanostars displaying broad plasmonic resonance and high surface-enhanced Raman sensitivity. Nanoscale. 2015;**7**(32):13629-13637. DOI: 10.1039/c5nr02819a

[110] He S, Kang MWC, Khan FJ, Tan EKM, Reyes MA, Kah JCY. Optimizing gold nanostars as a colloid-based surface-enhanced Raman scattering (SERS) substrate. Journal of Optics. 2015;**17**(11):114013. DOI: 10.1088/2040-8978/17/11/114013

[111] Kariuki VM, Hoffmeier JC, Yazgan I, Sadik OA. Seedless synthesis and SERS characterization of multi-branched gold nanoflowers using water soluble polymers. Nanoscale. 2017;**9**(24):8330-8340. DOI: 10.1039/c7nr01233k

[112] Tran V, Thiel C, Svejda JT, et al. Probing the SERS brightness of individual Au nanoparticles, hollow Au/Ag nanoshells, Au nanostars and Au core/Au satellite particles: Single-particle experiments and computer simulations. Nanoscale. 2018;**10**(46):21721-21731. DOI: 10.1039/c8nr06028b

[113] Choo P, Arenas-Esteban D, Jung I, et al. Investigating reaction intermediates during the seedless growth of gold Nanostars using electron tomography. ACS Nano. 2022;**16**(3):4408-4414. DOI: 10.1021/acsnano.1c10669

[114] Ahmed W, Demirtaş Ö, Öztürk İM, Bek A. Monolayer assembly of MultiSpiked gold nanoparticles for surface-enhanced Raman spectroscopy-based trace detection of dyes and explosives. ACS Applied Nano Materials. 2020;**3**(7):6766-6773. DOI: 10.1021/acsanm.0c01177

[115] Gellner M, Steinigeweg D, Ichilmann S, et al. 3D self-assembled

plasmonic superstructures of gold nanospheres: Synthesis and characterization at the single-particle level. Small. 2011;**7**(24):3445-3451. DOI: 10.1002/smll.201102009

[116] Yang J-K, Kang H, Lee H, et al. Single-step and rapid growth of silver nanoshells as SERS-active nanostructures for label-free detection of pesticides. ACS Applied Materials & Interfaces. 2014;**6**(15):12541-12549. DOI: 10.1021/am502435x

[117] McLellan JM, Li Z-Y, Siekkinen AR, Xia Y. The SERS activity of a supported Ag nanocube strongly depends on its orientation relative to laser polarization. Nano Letters. 2007;**7**(4):1013-1017. DOI: 10.1021/nl070157q

[118] Near R, Hayden S, El-Sayed M. Extinction vs absorption: Which is the indicator of Plasmonic field strength for silver Nanocubes? Journal of Physical Chemistry C. 2012;**116**(43):23019-23026. DOI: 10.1021/jp309272b

[119] Rycenga M, Langille MR, Personick ML, Ozel T, Mirkin CA. Chemically isolating hot spots on concave nanocubes. Nano Letters. 2012; **12**(12):6218-6222. DOI: 10.1021/ nl3032235

[120] Jeon HB, Tsalu PV, Ha JW. Shape effect on the refractive index sensitivity at localized surface Plasmon resonance inflection points of single gold Nanocubes with vertices. Scientific Reports. 2019;**9**(1):13635. DOI: 10.1038/ s41598-019-50032-3

[121] Xu P, Lu W, Zhang J, Zhang L. Efficient hydrolysis of ammonia borane for hydrogen evolution catalyzed by Plasmonic Ag@Pd Core–Shell Nanocubes. ACS Sustainable Chemistry & Engineering. 2020;**8**(33):12366-12377. DOI: 10.1021/acssuschemeng.0c02276

[122] Dong J, Yang C, Wu H, et al. Two-dimensional self-assembly of Au@Ag Core-Shell Nanocubes with different permutations for ultrasensitive SERS measurements. ACS Omega. 2022;**7**(4): 3312-3323. DOI: 10.1021/ acsomega.1c05452

[123] Kneipp K, Haka AS, Kneipp H, et al. Surface-enhanced Raman spectroscopy in single living cells using gold nanoparticles. Applied Spectroscopy. 2002;**56**(2): 150-154. DOI: 10.1366/0003702021954557

[124] Wustholz KL, Henry A-I, McMahon JM, et al. Structure-activity relationships in gold nanoparticle dimers and trimers for surface-enhanced Raman spectroscopy. Journal of the American Chemical Society. 2010;**132**(31): 10903-10910. DOI: 10.1021/ja104174m

[125] Gao Y, Zhang R, Cheng J-C, Liaw J-W, Ma C. Optical properties of plasmonic dimer, trimer, tetramer and pentamer assemblies of gold nanoboxes. Journal of Quantitative Spectroscopy and Radiative Transfer. 2013;**125**:23-32. DOI: 10.1016/j.jqsrt.2013.04.014

[126] Zohar N, Chuntonov L, Haran G. The simplest plasmonic molecules: Metal nanoparticle dimers and trimers. Journal of Photochemistry and Photobiology C: Photochemistry Reviews. 2014;**21**:26-39. DOI: 10.1016/j.jphotochemrev.2014. 10.002

[127] Sergiienko S, Moor K, Gudun K, Yelemessova Z, Bukasov R. Nanoparticle-nanoparticle vs. nanoparticle-substrate hot spot contributions to the SERS signal: Studying Raman labelled monomers, dimers and trimers. Physical Chemistry Chemical Physics. 2017;**19**(6): 4478-4487. DOI: 10.1039/c6cp08254h

[128] Nagarajan A, Panchanathan AP, Chelliah P, Satoh H, Inokawa H. FDTD

study on evolution of trimer silver@silica Nanospheres to dimer for SERS characteristics. Plasmonics. 2022;**17**(2):647-652. DOI: 10.1007/s11468-021-01554-y

[129] VAF. 2013 7th International Congress on Advanced Electromagnetic Materials in Microwaves and Optics (METAMATERIALS 2013): Bordeaux, France, 16–21 September 2013. Piscataway, NJ: IEEE; 2013

[130] Jin Q, Wang L, Yan S, Wei H, Huang Y. Plasmonic nano-tweezer based on square nanoplate tetramers. Applied Optics. 2018;**57**(19):5328-5332. DOI: 10.1364/AO.57.005328

[131] Xi C, Marina PF, Xia H, Wang D. Directed self-assembly of gold nanoparticles into plasmonic chains. Soft Matter. 2015;**11**(23):4562-4571. DOI: 10.1039/c5sm00900f

[132] Pocock SR, Xiao X, Huidobro PA, Giannini V. Topological Plasmonic chain with retardation and radiative effects. ACS Photonics. 2018;**5**(6):2271-2279. DOI: 10.1021/acsphotonics.8b00117

[133] Luo S, Mancini A, Wang F, Liu J, Maier SA, de Mello JC. High-throughput fabrication of triangular Nanogap arrays for surface-enhanced Raman spectroscopy. ACS Nano. 2022;**16**: 7438-7447. DOI: 10.1021/acsnano.1c09930

[134] Zhang C, Chen S, Jiang Z, Shi Z, Wang J, Du L. Highly sensitive and reproducible SERS substrates based on ordered micropyramid Array and silver nanoparticles. ACS Applied Materials & Interfaces. 2021;**13**(24):29222-29229. DOI: 10.1021/acsami.1c08712

[135] Lu Y-C, Chiang W-H, Liu C-Y, Chu JP, Ho H-C, Hsueh C-H. Wafer-scale SERS metallic nanotube arrays with highly ordered periodicity. Sensors and Actuators B: Chemical. 2021;**329**:129132. DOI: 10.1016/j.snb.2020.129132

[136] Kim J, Lee JS, Kim J-W, et al. Fabrication of plasmonic arrays of nanodisks and nanotriangles by nanotip indentation lithography and their optical properties. Nanoscale. 2021; **13**(8):4475-4484. DOI: 10.1039/d0nr08398d

[137] Choi M, Kim S, Choi SH, Park H-H, Byun KM. Highly reliable SERS substrate based on plasmonic hybrid coupling between gold nanoislands and periodic nanopillar arrays. Optics Express. 2020; **28**(3):3598-3606. DOI: 10.1364/OE.386726

[138] Kasani S, Curtin K, Wu N. A review of 2D and 3D plasmonic nanostructure array patterns: Fabrication, light management and sensing applications. Nano. 2019;**8**(12):2065-2089. DOI: 10.1515/nanoph-2019-0158

[139] Anikin K, Rodyakina E, Veber S, Milekhin A, Latyshev A, Zahn DRT. Localized surface Plasmon resonance in gold nanocluster arrays on opaque substrates. Plasmonics. 2019;**14**(6): 1527-1537. DOI: 10.1007/s11468-019-00949-2

[140] Brawley ZT, Bauman SJ, Darweesh AA, Debu DT, Tork Ladani F, Herzog JB. Plasmonic Au Array SERS substrate with optimized thin film oxide substrate layer. Materials (Basel). 2018; **11**(6):942. DOI: 10.3390/ma11060942

[141] Zhao Q, Yang H, Nie B, Luo Y, Shao J, Li G. Wafer-scale and cost-effective manufacturing of controllable Nanogap arrays for highly sensitive SERS sensing. ACS Applied Materials & Interfaces. 2022;**14**(2):3580-3590. DOI: 10.1021/acsami.1c22465

[142] Hu Y, Li L, Wang R, et al. High-speed parallel Plasmonic direct-writing nanolithography using Metasurface-based Plasmonic lens. Engineering. 2021;7(11):1623-1630. DOI: 10.1016/j.eng.2020.08.019

[143] Hulteen JC, van Duyne RP. Nanosphere lithography: A materials general fabrication process for periodic particle array surfaces. Journal of Vacuum Science & Technology A: Vacuum, Surfaces, and Films. 1995;13(3):1553-1558. DOI: 10.1116/1.579726

[144] Haynes CL, van Duyne RP. Nanosphere lithography: A versatile nanofabrication tool for studies of size-dependent nanoparticle optics. The Journal of Physical Chemistry. B. 2001;105(24):5599-5611. DOI: 10.1021/jp010657m

[145] Zhang C. Nanosphere Lithography and its Application in Rapid and Economic Fabrication of Plasmonic Hydrogenated Amorphous Silicon Photovoltaic Devices. MI, USA: Michigan Technological University; 2016

[146] Rahaman M, Moras S, He L, Madeira TI, Zahn DRT. Fine-tuning of localized surface plasmon resonance of metal nanostructures from near-infrared to blue prepared by nanosphere lithography. Journal of Applied Physics. 2020;128(23):233104. DOI: 10.1063/5.0027139

[147] Kahraman M, Daggumati P, Kurtulus O, Seker E, Wachsmann-Hogiu S. Fabrication and characterization of flexible and tunable plasmonic nanostructures. Scientific Reports. 2013;3:3396. DOI: 10.1038/srep03396

[148] Liu Y, Li X, Cheng J, et al. SERS devices with "hedgehog-like" nanosphere arrays for detection of trace pesticides. Journal of Innovative Optical

Health Sciences. 2021;14(04):2141005. DOI: 10.1142/S1793545821410054

[149] Rahaman M, Aslam MA, He L, Madeira TI, Zahn DRT. Plasmonic hot electron induced layer dependent anomalous Fröhlich interaction in InSe. Communications on Physics. 2021;4(1):172. DOI: 10.1038/s42005-021-00674-5

[150] Cao Y, Sun M. Tip-enhanced Raman spectroscopy. Reviews in Physics. 2022;8:100067. DOI: 10.1016/j.revip.2022.100067

[151] Gersten J, Nitzan A. Electromagnetic theory of enhanced Raman scattering by molecules adsorbed on rough surfaces. The Journal of Chemical Physics. 1980;73(7):3023-3037. DOI: 10.1063/1.440560

[152] Liao PF, Wokaun A. Lightning rod effect in surface enhanced Raman scattering. The Journal of Chemical Physics. 1982;76(1):751-752. DOI: 10.1063/1.442690

[153] Richard-Lacroix M, Zhang Y, Dong Z, Deckert V. Mastering high resolution tip-enhanced Raman spectroscopy: Towards a shift of perception. Chemical Society Reviews. 2017;46(13):3922-3944. DOI: 10.1039/c7cs00203c

[154] Trautmann S, Aizpurua J, Götz I, et al. A classical description of subnanometer resolution by atomic features in metallic structures. Nanoscale. 2017;9(1):391-401. DOI: 10.1039/c6nr07560f

[155] Zhang W, Cui X, Martin OJF. Local field enhancement of an infinite conical metal tip illuminated by a focused beam. Journal of Raman Specroscopy. 2009;40(10):1338-1342. DOI: 10.1002/jrs.2439

[156] Huang T-X, Huang S-C, Li M-H, Zeng Z-C, Wang X, Ren B. Tip-enhanced Raman spectroscopy: Tip-related issues. Analytical and Bioanalytical Chemistry. 2015;**407**(27):8177-8195. DOI: 10.1007/s00216-015-8968-8

[157] Fleischer M. Near-field scanning optical microscopy nanoprobes. Nanotechnology Reviews. 2012;**1**(4):313-338. DOI: 10.1515/ntrev-2012-0027

[158] Yang B, Kazuma E, Yokota Y, Kim Y. Fabrication of sharp gold tips by three-electrode electrochemical etching with high controllability and reproducibility. Journal of Physical Chemistry C. 2018;**122**(29):16950-16955. DOI: 10.1021/acs.jpcc.8b04078

[159] Foti A, Barreca F, Fazio E, et al. Low cost tips for tip-enhanced Raman spectroscopy fabricated by two-step electrochemical etching of 125 μm diameter gold wires. Beilstein Journal of Nanotechnology. 2018;**9**:2718-2729. DOI: 10.3762/bjnano.9.254

[160] Lopes M, Toury T, La Chapelle ML, de, Bonaccorso F, Gucciardi PG. Fast and reliable fabrication of gold tips with sub-50 nm radius of curvature for tip-enhanced Raman spectroscopy. The Review of Scientific Instruments. 2013;**84**(7):73702. DOI: 10.1063/1.4812365

[161] Yang L-K, Huang T-X, Zeng Z-C, et al. Rational fabrication of a gold-coated AFM TERS tip by pulsed electrodeposition. Nanoscale. 2015;**7**(43):18225-18231. DOI: 10.1039/c5nr04263a

[162] Huang T-X, Li C-W, Yang L-K, et al. Rational fabrication of silver-coated AFM TERS tips with a high enhancement and long lifetime. Nanoscale. 2018;**10**(9):4398-4405. DOI: 10.1039/c7nr08186c

[163] Park C-G, Kim J-Y, Lee E-B, et al. Tip-enhanced Raman scattering with a nanoparticle-functionalized probe. Bulletin of the Korean Chemical Society. 2012;**33**(5):1748-1752. DOI: 10.5012/bkcs.2012.33.5.1748

[164] Wang D, Zhang Z, Wang J, Ma K, Gao H, Wang X. Nanofocusing performance of plasmonic probes based on gradient permittivity materials. Journal of Optics. 2022;**24**(6):65003. DOI: 10.1088/2040-8986/ac69f6

[165] Zhang K, Bao Y, Cao M, et al. Low-background tip-enhanced Raman spectroscopy enabled by a Plasmon thin-film waveguide probe. Analytical Chemistry. 2021;**93**(21):7699-7706. DOI: 10.1021/acs.analchem.1c00806

[166] Sanders A, Bowman RW, Zhang L, et al. Understanding the plasmonics of nanostructured atomic force microscopy tips. Applied Physics Letters. 2016;**109**(15):153110. DOI: 10.1063/1.4964601

[167] Pettinger B, Domke KF, Zhang D, Picardi G, Schuster R. Tip-enhanced Raman scattering: Influence of the tip-surface geometry on optical resonance and enhancement. Surface Science. 2009;**603**(10–12):1335-1341. DOI: 10.1016/j.susc.2008.08.033

[168] Xu H, Bjerneld EJ, Aizpurua J, et al. Interparticle coupling effects in surface-enhanced Raman scattering. Journal of Gastroenterology and Hepatology. 2008;**23**(5):35-42. DOI: 10.1117/12.430771

[169] Yang Z, Aizpurua J, Xu H. Electromagnetic field enhancement in TERS configurations. Journal of Raman Specroscopy. 2009;**40**(10):1343-1348. DOI: 10.1002/jrs.2429

[170] He L, Rahaman M, Madeira TI, Zahn DRT. Understanding the role of different substrate geometries for

achieving optimum tip-enhanced Raman scattering sensitivity. Nanomaterials (Basel). 2021;**11**(2):376. DOI: 10.3390/nano11020376

[171] Politano A, Formoso V, Chiarello G. Dispersion and damping of gold surface Plasmon. Plasmonics. 2008;**3**(4): 165-170. DOI: 10.1007/s11468-008-9070-2

[172] Madoyan KK, Melikyan AH, Minassian HR. Radiation damping of surface Plasmons in a pair of nanoparticles and in nanoparticles near interfaces. Journal of Physical Chemistry C. 2012;**116**(31):16800-16805. DOI: 10.1021/jp305144u

[173] Kolwas K, Derkachova A. Damping rates of surface plasmons for particles of size from nano- to micrometers; reduction of the nonradiative decay. Journal of Quantitative Spectroscopy and Radiative Transfer. 2013;**114**:45-55. DOI: 10.1016/j.jqsrt.2012.08.007

[174] Milekhin AG, Rahaman M, Rodyakina EE, Latyshev AV, Dzhagan VM, Zahn DRT. Giant gap-plasmon tip-enhanced Raman scattering of MoS2 monolayers on Au nanocluster arrays. Nanoscale. 2018;**10**(6):2755-2763. DOI: 10.1039/c7nr06640f

[175] Liao M, Jiang S, Hu C, et al. Tip-enhanced Raman spectroscopic imaging of individual carbon nanotubes with subnanometer resolution. Nano Letters. 2016;**16**(7):4040-4046. DOI: 10.1021/acs.nanolett.6b00533